EARTHARXIV | PREPRINT COVERSHEET

Transition from buoyancy-driven to shear-driven melting in a buoyant plume at a vertical ice face

Yuchen Ma[1], Paul R. Holland[2], Ken X. Zhao[3], Jonathan D. Nash[4], Pierre Dutrieux[2], Christina Schmidt[2], and John R. Taylor[1,*]

[1] Department of Applied Mathematics and Theoretical Physics, University of Cambridge, Wilberforce Road, Cambridge CB3 0WA, UK

[2] British Antarctic Survey, High Cross, Madingley Road, Cambridge CB3 0ET, UK

[3] Department of Earth, Marine and Environmental Sciences, University of North Carolina at Chapel Hill, Chapel Hill, NC 27599, USA

[4] College of Earth, Ocean, and Atmospheric Sciences, Oregon State University, Corvallis, OR 97331, USA

Author email addresses

Yuchen Ma	ym460@cam.ac.uk
Paul R. Holland	pahol@bas.ac.uk
Ken X. Zhao	kenzhao@unc.edu
Jonathan D. Nash	jonathan.nash@oregonstate.edu
Pierre Dutrieux	pitr1@bas.ac.uk
Christina Schmidt	christina.schmidt@bas.ac.uk
John R. Taylor *	J.R.Taylor@damtp.cam.ac.uk

* Corresponding author

Preprint and peer-review status

This manuscript is a non-peer-reviewed preprint submitted to EarthArXiv. It has been submitted to the *Journal of Fluid Mechanics* for peer review.

Banner appropriate to article type will appear here in typeset article

Transition from buoyancy-driven to shear-driven melting in a buoyant plume at a vertical ice face

Yuchen Ma[1], Paul R. Holland[2], Ken X. Zhao[3], Jonathan D. Nash[4], Pierre Dutrieux[2], Christina Schmidt[2], and John R. Taylor[1]

[1]Department of Applied Mathematics and Theoretical Physics, University of Cambridge, Wilberforce Road, Cambridge CB3 0WA, UK

[2]British Antarctic Survey, High Cross, Madingley Road, Cambridge CB3 0ET, UK

[3]Department of Earth, Marine and Environmental Sciences, University of North Carolina at Chapel Hill, Chapel Hill, NC 27599, USA

[4]College of Earth, Ocean, and Atmospheric Sciences, Oregon State University, Corvallis, OR 97331, USA

Corresponding author: John Taylor, jrt51@cam.ac.uk

(Received xx; revised xx; accepted xx)

Melting of a vertical ice face in otherwise quiescent saline water generates a buoyant plume that rises along the ice. Heat and salt transfer through the thin near-wall boundary layers controls the melt rate and must be parameterized in models that do not resolve these layers. In plume models, the three-equation framework of Holland & Jenkins (1999) is commonly coupled to transfer laws based on plume-induced shear. Under weak-shear conditions, however, laboratory experiments and simulations show that melting is controlled by buoyancy-driven convection and is approximately independent of plume velocity. Here, we develop a boundary-layer theory that unifies these two transfer regimes. The melt rate is set by the boundary-layer thicknesses, which in turn is governed by two competing length scales: a viscous length and a buoyancy viscous length scale. The resulting flux laws recover existing shear-driven and buoyancy-driven models as limits, retain the algebraic structure of the three-equation model, and predict a regime transition when the two length scales become comparable, corresponding to a plume velocity of roughly 6-8 cm/s for typical fjord conditions. We test the theory using large-eddy simulations that resolve the diffusive sublayers adjacent to a melting vertical ice face. In these simulations a melt-driven plume starts in the buoyancy-driven regime and transitions into the shear-driven regime. The melt rates across the transition are well described by the unified theory.

Key words:

Abstract must not spill onto p.2

1. Introduction

Buoyant plumes along ice–ocean interfaces entrain ambient seawater and transport heat towards the ice, influencing submarine melting. These flows are particularly relevant at marine-terminating glaciers in Greenland fjords: mass loss from the Greenland Ice Sheet is a leading contributor to global sea-level rise, and a substantial fraction of this loss occurs at marine-terminating glaciers in narrow fjords (Mouginot *et al.* 2019). In these fjords, relatively warm and salty fjord water comes into contact with the ice, and two types of buoyant plume might exist. The first are vigorous but localized *subglacial discharge plumes*, which are fed by surface meltwater that drains through the glacier and enters the fjord at depth. These plumes typically have velocities of order 0.1–1 $\mathrm{m\,s^{-1}}$ and widths of order 100 m (Jackson *et al.* 2017; Hewitt 2020). The second are much weaker, spatially distributed *meltwater plumes*, which are driven by submarine melting of the ice face itself. They typically have velocities of order 0.03 $\mathrm{m\,s^{-1}}$ and thicknesses of order 1 m or less (Kimura *et al.* 2014; Magorrian & Wells 2016; Nash *et al.* 2024). Both plume types entrain ambient warm seawater and enhance melting of glaciers. In natural glacier settings, calving (Shaya *et al.* 2025) and internal waves (Cusack *et al.* 2023) can also energize the ice–ocean boundary layer, such that melting need not be driven primarily by local meltwater buoyancy. In this study, we focus on melting associated with buoyant plumes. Some of the dynamics explored here may also be relevant to situations in which the boundary layer kinetic energy is supplied primarily by external flows, as observed by Weiss *et al.* (2026).

The melt rate associated with both plume types is controlled by the thin ocean boundary layer, which is millimetres thick and has to be modelled. The standard approach to parameterize the melt rate in ocean models is the 'three-equation' model of Holland & Jenkins (1999), in which the turbulent fluxes of heat and salt toward the ice are proportional to the friction velocity u_*. The physical picture underlying this closure is the shear-driven turbulence boundary layer theory, originally developed from turbulence measurements in the boundary layer beneath drifting sea ice (McPhee *et al.* 1987). This closure is well supported at near-horizontal interfaces beneath sea ice and ice shelves, where the shear is supplied by tides, mean currents or the drift of the ice itself, by observations (Jenkins *et al.* 2010) and by turbulence-resolving simulations (Vreugdenhil & Taylor 2019; Vreugdenhil *et al.* 2022). At a near-vertical ice–ocean interface, this parameterization is appropriate when the plume velocity is strong, but may substantially underestimate the melt rate when the plume velocity is weak, a regime commonly associated with meltwater plumes (McConnochie & Kerr 2017; Zhao *et al.* 2026).

When the plume velocity is weak, turbulence near the ice is created through the vertical buoyancy flux instead of shear production. This scenario is closely related to the natural convection boundary layer (NCBL) along a heated vertical wall, whose structure has been characterized by theory (George & Capp 1979), laboratory measurements (Cheesewright 1968; Tsuji & Nagano 1988, 1989) and direct numerical simulations (DNS) (Versteegh & Nieuwstadt 1999; Ng *et al.* 2015; Nakao *et al.* 2017; Ke *et al.* 2020; Howland *et al.* 2023). Building on the flux scalings established for the NCBL, Kerr & McConnochie (2015) developed a model for this regime, in which the melt rate is controlled by the buoyancy anomaly at the interface and is independent of the plume velocity. This model reproduces the melt rates and interface temperatures measured in laboratory experiments on melting vertical solid surfaces, and is further supported by DNS of a melting vertical ice face (Gayen *et al.* 2016).

For brevity, we refer to the shear-driven three-equation closure of Holland & Jenkins (1999) as the HJ model, and to the velocity-independent, buoyancy-driven model of Kerr & McConnochie (2015) as the KM model. The transition between these two models is

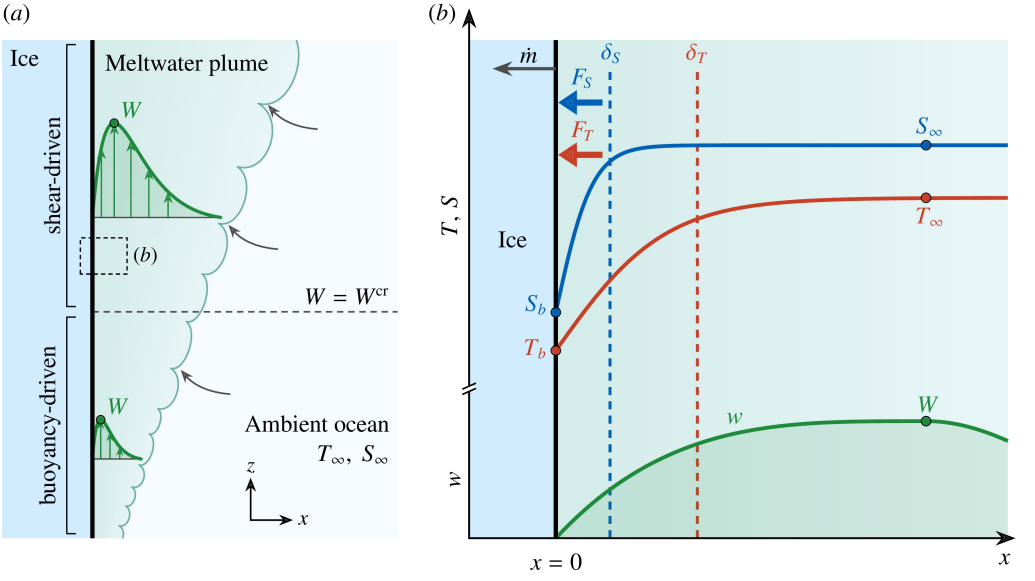


Figure 1. Schematic of a buoyant plume at a vertical ice face, where x is the wall-normal coordinate and z the along-face coordinate in the direction of the plume. (*a*) The plume rises along the ice, entraining ambient water of temperature T_∞ and salinity S_∞, and accelerates with height; W is the maximum of its velocity profile $w(x)$. The ice-ocean boundary layer is buoyancy-driven where the plume is weak and becomes shear-driven once W exceeds the transition velocity W^{cr}. (*b*) Structure of the boundary layer in the region marked in (*a*), which is common to both regimes. Salinity S (blue) and temperature T (red) increase from their interface values S_b and T_b to the ambient values S_∞ and T_∞ across diffusive sublayers of thickness δ_S and δ_T (dashed lines), while the vertical velocity w (green) increases from zero at the ice to the plume velocity W. The wall-normal fluxes of salt F_S and heat F_T (arrows) are directed towards the interface and sustain the melt rate $\dot{m}$, expressed as an ice-equivalent thickness per unit time. The horizontal axis is not to scale, in order to highlight the boundary-layer structure.

most clearly illustrated in Figure 1a. Initially, when the plume is very weak, melting is controlled primarily by buoyancy, and the melt rate is well described by the KM model and is independent of the plume velocity W. If the plume accelerates and W exceeds the transition velocity W_{cr}, the melt rate becomes velocity-dependent and the shear-driven HJ model becomes an accurate description of the melt rate.

Conditions at real glacier fronts are understood to span both the KM and the HJ regimes, although direct observational constrains remain limited. Within subglacial discharge plumes plume velocities can reach 1–3 $\mathrm{m\,s^{-1}}$ (Ovall *et al.* 2025), where the HJ model holds. Away from discharge outlets the plume velocity is weak, and there the HJ model, driven by the upwelling velocity of the melt plume alone, underpredicts observed melt rates by one to two orders of magnitude (Sutherland *et al.* 2019; Jackson *et al.* 2020). Part of this gap is unresolved horizontal flow (Jackson *et al.* 2020), but direct measurements at near-vertical ice faces reveal a more basic failure of the HJ model: observed melt rates become independent of velocity below roughly $0.04\,\mathrm{m\,s^{-1}}$ (Weiss *et al.* 2025; McConnochie & Kerr 2017), where buoyant meltwater plumes dominate the near-boundary turbulence (Nash *et al.* 2024). A shear-driven model with constant coefficients cannot produce a melt rate that stays finite as the velocity vanishes. What these observations call for is a single model that captures both the KM and the HJ regimes and, crucially, the transition between them.

Efforts to model the transition from the buoyancy-driven regime to the shear-driven regime in a meltwater plume date back to Wells & Worster (2008), who predicted that the transition occurs at a critical value of the Rayleigh number $Ra_z = \Delta b\, z^3/(\nu\kappa)$, where z is the distance from the origin of the plume and κ the relevant diffusivity and $\Delta b = g(\rho_\infty - \rho_b)/\rho_0$ the buoyancy anomaly caused by different densities between the far-field water ρ_∞ and the ice-ocean interface ρ_b (also referred to as reduced gravity by Wells & Worster (2008).) Based on the scaling theory of Rayleigh–Bénard convection (Grossmann & Lohse 2000), Kerr & McConnochie (2015) proposed a critical Rayleigh number of $Ra_c \approx 10^{21}$ for the transition. McConnochie & Kerr (2017) subsequently used an empirical plume scaling law derived from laboratory experiments to translate this criterion into a threshold velocity of 0.04 m s^{-1} under laboratory conditions. Beyond the context of idealised simulations and lab experiments, the distance from the plume origin, z, is somewhat ambiguous. In reality, the plume at a given height depends on the upstream evolution of the entire plume, whose information is often hard or impossible to know, particularly when the geometry of the ice face is complex. What is still lacking is a local theory that predicts the transition from the local properties of the flow.

Despite the lack of a predictive local theory for the transition, simplified melt parameterizations spanning both regimes have recently been proposed (Schulz *et al.* 2022; Zhao *et al.* 2024, 2026). In these parameterizations, the melt rate is effectively taken to be the larger of the HJ and KM predictions, so that a transition velocity emerges naturally as the velocity at which the two models agree. Of these studies, Zhao *et al.* (2026) resolves the transition itself, using direct numerical simulations across a range of externally imposed velocities, stratifications and wall slopes. However, the behaviour of the melt rate near the transition velocity, and the near-wall mechanism governing the crossover, remain unexplained.

Two questions therefore arise, and they motivate this paper: (i) can we build a predictive theoretical model for the transition between two regimes of buoyant plumes? (ii) can we properly parameterize the melt rate behavior across the transition in a single unified model? We address both questions first with a unified boundary-layer theory, and then test its predictions against boundary-layer-resolving simulations.

We first develop a boundary-layer theory for the vertical ice-ocean interfaces of buoyant plumes (§ 2). After reviewing the HJ and KM models, we show that they can be recast as statements about a near-wall turbulent diffusivity that grows as the cube of the distance from the ice and thereby sets the thickness of the diffusive sublayers controlling the melt rate. The magnitude of this diffusivity is fixed by one of two length scales, the viscous scale $l_\nu = \nu/u_*$ under shear-driven turbulence (where ν is the kinematic viscosity of seawater, u_* is the friction velocity), and the buoyancy-viscous scale $l_b = (\nu^2/\Delta b)^{1/3}$ under buoyancy-driven convection. Combining the two scales yields unified flux laws that recover the KM model when $l_b \ll l_\nu$, recover the HJ model when $l_\nu \ll l_b$, and predict a transition at $u_* \sim (\nu\,\Delta b)^{1/3}$, a plume velocity of 0.06–0.08 m s^{-1}.

We then test the theory with LES of the meltwater plume that resolves the diffusive sublayers at a melting vertical ice face (§ 3). Experiments and simulations to date have concentrated on the buoyancy-driven limit, and to our knowledge, the shear-driven regime developed from these meltwater plumes has not previously been realized in the laboratory or in wall-resolved simulations. Following the temporally evolving configuration for natural convection boundary layers used by Ke *et al.* (2020) (see also Ke *et al.* 2021, 2023), we apply periodic boundary conditions in the along-ice direction, which converts the spatial development of the meltwater plume with height into temporal evolution. These simulations successfully capture the transition across different flow regimes, and the predicted melt rates are consistent with the theoretical model.

 Focus on Fluids articles must not exceed this page length

The remainder of the paper is organized as follows. Section 2 reviews the shear-driven (§ 2.1) and buoyancy-driven (§ 2.2) models and develops the unified boundary-layer theory (§ 2.3). Section 3 describes the LES configuration (§ 3.1), documents the regime transition (§ 3.3) and tests the theory against the simulations (§ 3.4). Implications for ocean and fjord modelling are discussed together with the conclusions in § 4.

2. A unified parameterization scheme at a vertical ice-ocean interface

In this section we review the two existing melt rate parameterizations and their underlying assumptions, before discussing the unified parameterization scheme. All of these parameterization schemes share the same idealized thermal and haline boundary layer structures, as sketched in Figure 1(b), where x is the wall-normal coordinate (zero at the interface, increasing into the ocean), z is the along-face coordinate in the direction of the plume, and y is the horizontal along-face direction, with velocity components (u, v, w).

We consider a buoyant plume rising through a quiescent ambient, with no externally imposed current. The boundary layer is taken to be statistically steady and homogeneous along the ice, so that mean quantities depend on x alone and the wall-normal fluxes of heat and salt are independent of x because there are no divergence/convergence of fluxes in a steady state. We denote these fluxes as F_T, F_S, the ambient (far-field) temperature and salinity by T_∞ and S_∞, their values at the ice-ocean interface by T_b and S_b, and the melt rate, expressed as an ice-equivalent thickness per unit time, by $\dot{m}$. Strictly, the boundary layer responds to the temperature and salinity inside the plume, rather than to the far-field values. For the meltwater plumes simulated in § 3 the two are close: the difference is less than 1 % of $S_\infty - S_b$ for salinity and about 10 % of $T_\infty - T_b$ for temperature, and for simplicity we do not distinguish between them. For a subglacial discharge plume, which is much fresher and colder than the ambient, the difference is not negligible, and T_∞ and S_∞ (and hence Δb) should be taken as the plume values, as in plume models (Jenkins 2011).

All of the parameterizations considered here share the same interface thermodynamics: a linearized liquidus constraint together with conservation laws for heat and salt at the interface (Holland & Jenkins 1999),

$$\begin{cases} T_b = \lambda_1 S_b + \lambda_2 + \lambda_3 P, & (2.1a) \\ \rho_i L\, \dot{m} = \rho_w c_w\, F_T, & (2.1b) \\ \rho_i S_b\, \dot{m} = \rho_w\, F_S. & (2.1c) \end{cases}$$

Here ρ_w and ρ_i are the densities of seawater and ice, c_w is the specific heat capacity of seawater, L is the latent heat of fusion, and P is the sea water pressure. The liquidus coefficients λ_1, λ_2,λ_3 are linearized expression for the freezing point of seawater (Jenkins 2011). Equation (2.1b) represents the balance of the latent heat consumed by melting against the turbulent heat flux supplied by the ocean, neglecting heat conduction into the ice, and (2.1c) states that melting dilutes the interface salinity with the ice assumed to be salt-free. Throughout, we also neglect the slow retreat of the interface produced by melting itself: the melt velocity ($\dot{m} \sim 10^{-6}$ m s^{-1}) is orders of magnitude smaller than the boundary-layer velocities, so the retreat of the interface does not enter the flow and appears only through the interface conditions (2.1).

Given the ambient state (T_∞, S_∞), (2.1) constitutes three equations for the five unknowns $(T_b, S_b, F_T, F_S, \dot{m})$; a melt parameterization is therefore closed by supplying flux laws relating F_T and F_S to the temperature and salinity differences across the boundary layer. The parameterizations reviewed below differ only in these flux laws.

2.1. *The shear-driven regime: the three-equation (HJ) model*

Holland & Jenkins (1999) model the turbulent fluxes as proportional to the friction velocity $u_* \equiv \sqrt{\tau/\rho_0}$, where τ is shear stress at the ice-ocean interface and ρ_0 a reference density (the HJ model). This leads to the 'three-equation model' when combined with scaling expressions for the heat and salt flux:

$$F_T = \Gamma_T\, u_*\, (T_\infty - T_b), \qquad F_S = \Gamma_S\, u_*\, (S_\infty - S_b), \tag{2.2}$$

where Γ_T and Γ_S are dimensionless transfer coefficients. The HJ model further assumes a quadratic drag law relating the turbulent Reynold stress τ_u to the flow velocity, with a constant drag coefficient C_d. For the plume system, the friction velocity u_* is therefore given by

$$u_* = \sqrt{\frac{\tau_u}{\rho_0}} = \sqrt{C_d}\, W, \tag{2.3}$$

where W is the plume velocity and ρ_0 is the reference density. It should be noticed that at a vertical interface the wall stress at the ice τ_{wall} does not equal to the turbulent Reynold stress τ_u outside the viscous layer, because part of the interfacial stress supports the buoyancy of the fluid next to the ice. In this paper u_* is based on the turbulent stress τ_u, which is the one that follows (2.3), as shown in § 3.3.

The physical picture underlying (2.2) is a forced turbulent boundary layer: heat and salt are transferred by shear-driven turbulence, whose intensity is represented by the friction velocity u_*. The non-dimensional transfer coefficients Γ_T and Γ_S can, in principle, be derived from the theoretical wall-layer model of Kader & Yaglom (1972), but in practice they are most often calibrated against observations (Jenkins *et al.* 2010; Weiss *et al.* 2025). A limitation of this formulation is that the predicted melt rate vanishes in the absence of plume velocity, and so it underestimates melting in the weak-flow limit, where turbulence is buoyancy-driven.

2.2. *The buoyancy-driven regime: the convective (KM) model*

In the limit of weak plume velocity, the buoyancy input from melting drives turbulence directly. Meltwater is fresh and cold; at temperature typical of the polar oceans the freshening dominates, so that fluid adjacent to the ice is buoyant, with an interface buoyancy anomaly

$$\Delta b = g\frac{\rho_\infty - \rho_b}{\rho_0} = g\,[\beta\,(S_\infty - S_b) - \alpha\,(T_\infty - T_b)] \approx g\beta\,(S_\infty - S_b) > 0, \tag{2.4}$$

where α and β are the thermal expansion and haline contraction coefficients in the linear equation of state, and T_∞ and S_∞ are the far-field temperature and salinity, respectively.

Kerr & McConnochie (2015) developed a model for melting in this regime (the KM model), building on the classical measurements of turbulent natural convection at a heated vertical wall (Warner & Arpaci 1968; Cheesewright 1968; Tsuji & Nagano 1988), which are well described by the one-third power law

$$Nu = \gamma\, Ra^{1/3}, \qquad Nu = \frac{F_T H}{\kappa_T\, \Delta T}, \qquad Ra = \frac{g\alpha\, \Delta T\, H^3}{\kappa_T \nu}, \tag{2.5}$$

with H the height of the wall and $\gamma \approx 0.1$ a measured constant. At a melting ice face the buoyancy anomaly (2.4) is dominated by the salinity difference, so salinity takes over the role that temperature plays at a heated wall. KM therefore replaced the temperature terms in (2.5) with the corresponding terms in salinity: $\kappa_T \to \kappa_S$, $\Delta T \to \Delta S \equiv S_\infty - S_b$, $F_T \to F_S$, $g\alpha\, \Delta T \to \Delta b$, solving which for the flux then gives

$$F_S = \gamma\, \nu^{-1/3}\, \kappa_S^{2/3}\, \Delta b^{1/3}\, (S_\infty - S_b). \tag{2.6}$$

Note that F_S is independent of H, implying that the salt flux is independent of the wall height and of the position along the wall, a direct consequence of the one-third exponent.

The heat flux follows from the structure of the diffusive sublayers. In a quasi-steady boundary layer the wall-normal fluxes of heat and salt are independent of distance from the wall, so the turbulent fluxes in the outer layer equal the molecular fluxes across the diffusive sublayers adjacent to the ice. Since most of the variation of T and S occurs within these sublayers (a good approximation at large $Pr \equiv \nu/\kappa_T$ and $Sc \equiv \nu/\kappa_S$), the fluxes are assumed to be set by the sublayer thicknesses,

$$F_T \approx \kappa_T\, \frac{T_\infty - T_b}{\delta_T}, \qquad F_S \approx \kappa_S\, \frac{S_\infty - S_b}{\delta_S}, \qquad \frac{F_T}{F_S} \approx \frac{\kappa_T}{\kappa_S}\, \frac{T_\infty - T_b}{S_\infty - S_b}\, \frac{\delta_S}{\delta_T} \tag{2.7}$$

KM obtained the sublayer thicknesses ratio (δ_T/δ_S) from a surface-renewal description: they assumed that the sublayers grow diffusively, $\delta_T \sim \sqrt{\kappa_T t}$ and $\delta_S \sim \sqrt{\kappa_S t}$, until they are swept away by the convective eddies at some time Δt, so that their thicknesses is set by diffusion alone:

$$\frac{\delta_T}{\delta_S} = \left(\frac{\kappa_T}{\kappa_S}\right)^{1/2} = Le^{1/2}, \tag{2.8}$$

where $Le = \kappa_T/\kappa_S$ is the Lewis number. Combining (2.6)–(2.8) gives

$$F_T = \gamma\, \nu^{-1/3}\, \kappa_T^{1/2}\, \kappa_S^{1/6}\, \Delta b^{1/3}\, (T_\infty - T_b). \tag{2.9}$$

The physical picture described by the KM model is that convective turbulence, driven by salinity, sets the magnitude of the fluxes through (2.6), whereas the partition between heat and salt is set by molecular diffusion alone through (2.8). Equations (2.1), (2.6) and (2.9) form a closed system that represents meltrate in the buoyancy-driven regime.

The KM model is supported by melt rates and interface temperatures measured in the laboratory (Josberger & Martin 1981; Kerr & McConnochie 2015). The closed KM model predicts the measured melt rates to within about 10 %, and the same quantities are reproduced by DNS of a melting vertical ice face (Gayen *et al.* 2016).

2.3. *A unified boundary-layer theory*

Neither of the two models above captures the full range of plume velocities: the HJ model fails at low velocities and the KM model cannot capture the enhancement of melting by a strong plume velocity. We therefore seek a single set of flux laws containing both limits.

The difficulty in directly connecting the two models comes from the very different ways in which they were originally framed. Here, we frame both models as statements about the diffusive sublayers of temperature and salinity, whose thicknesses are set by the profile of the near-wall turbulent diffusivity. This common framework allows shear-driven turbulence and convection to contribute jointly to the turbulent diffusivity.

2.3.1. *Fluxes controlled by the diffusive sublayers*

As has been widely recognized in previous studies (Kerr & McConnochie 2015; Gayen *et al.* 2016; Howland *et al.* 2023), the fluxes delivered to the ice are controlled by thin diffusive sublayers of temperature and salinity, within which turbulent motions are suppressed by the boundary and the wall-normal transport of heat and salt is carried by molecular diffusion. To make this precise, we decompose the mean wall-normal fluxes into molecular and turbulent contributions. We use $\overline{(\cdot)}$ to denote an average over time and the directions

parallel to the ice (over a scale that is large compared to the turbulent motions but small compared to variations in outer layer properties) and primes for the fluctuations about this average; F_T and F_S are defined as positive when directed towards the ice. Then

$$F_T = \kappa_T \, \partial_x \overline{T} - \overline{u'T'} = \left(\kappa_T + K_T^{\mathrm{turb}}(x)\right) \partial_x \overline{T}, \tag{2.10}$$

where the turbulent flux has been modelled with an eddy diffusivity acting on the mean gradient, $-\overline{u'T'} = K_T^{\mathrm{turb}}(x) \, \partial_x \overline{T}$, and likewise for F_S with $K_S^{\mathrm{turb}}(x)$. Since F_T is independent of x, only its partition between the molecular and turbulent terms varies with distance from the wall. The turbulent diffusivities, K_T^{turb} and K_S^{turb}, vanish at the ice and increase outward, and hence the total diffusivity is molecular next to the ice, while the turbulent diffusivity dominates outside of the diffusive sublayers. We define the diffusive sublayer edge as the position where the two are equal (Howland *et al.* 2023),

$$K_T^{\mathrm{turb}}(\delta_T) = \kappa_T, \qquad K_S^{\mathrm{turb}}(\delta_S) = \kappa_S. \tag{2.11}$$

Other definitions of δ_T and δ_S used in the literature (e.g. Kerr & McConnochie (2015)) are essentially consistent with this.

Because the Prandtl number $Pr \equiv \nu/\kappa_T$ and the Schmidt number $Sc = \nu/\kappa_S$ are large, the sublayers are thin and the mean gradients within them are much steeper than outside, so most of the temperature and salinity difference across the boundary layer is taken up within $x \lesssim \delta_T, \delta_S$, where transport is predominantly molecular. The fluxes therefore scale as

$$F_T \sim \kappa_T \, \frac{T_\infty - T_b}{\delta_T}, \qquad F_S \sim \kappa_S \, \frac{S_\infty - S_b}{\delta_S}. \tag{2.12}$$

The $\sim$ sign acknowledges an order-one prefactor with two contributions: turbulent transport already contributes somewhat within the sublayer, and part of the temperature and salinity difference is taken up outside it, for instance in the logarithmic layers that develop beyond the sublayer (Kader & Yaglom 1972; Tsuji & Nagano 1988). Both are order-one corrections and are absorbed into the constants of the flux laws below. The problem of predicting the melt rate is thus reduced to predicting the sublayer thicknesses: given a model for $K_T^{\mathrm{turb}}(x)$ and $K_S^{\mathrm{turb}}(x)$, (2.11) fixes δ_T and δ_S, and (2.12) then gives the fluxes.

2.3.2. *Near-ice turbulent diffusivity: shear and buoyancy contributions*

Our central assumption is that, close to the ice, the turbulent diffusivities grow as the cube of the distance from the ice:

$$K_T, K_S \propto x^3. \tag{2.13}$$

This is a well-known result for near-wall turbulence: a cubic near-wall eddy diffusivity was proposed as early as Murphree (1932), was placed on an asymptotic footing by Monin & Yaglom (1971) and Chapman & Kuhn (1986), underlies the high-Pr, high-Sc transfer laws of Kader & Yaglom (1972), and has been confirmed directly in numerical simulations of near-wall scalar transport (Kasagi *et al.* 1992; Schwertfirm & Manhart 2007).

The underlying reason for the cubic dependence can be seen by expanding the fluctuating fields about the interface. The wall-normal velocity fluctuation u' vanishes to second order: its value at the ice is zero by impermeability, and its wall-normal derivative also vanishes since continuity gives $\partial_x u' = -\partial_y v' - \partial_z w'$ while the tangential velocities v' and w' are identically zero everywhere on the ice by no-slip. Therefore, the wall-normal velocity fluctuation scales as $u' \propto x^2$. The scalar fluctuations, by contrast, vanish only to first order: the interface fixes the scalar values, so $T'(0) = S'(0) = 0$, but their wall-normal gradients (the fluctuating diffusive fluxes) need not vanish, giving $T', S' \propto x$. Note that the interface

conditions (2.1) are more complicated than fixed-value conditions, but because T_b and S_b vary only weakly they are close to Dirichlet in practice. The turbulent fluxes therefore grow as $\overline{u'T'}$, $\overline{u'S'} \propto x^3$, and since the mean gradients $\overline{T}_x$, $\overline{S}_x$ are approximately uniform across the diffusive sublayers (except for at the edge of the boundary layer), the turbulent diffusivities inherit the cubic form (2.13) close to the ice.

For forced (shear-driven) wall turbulence, the length scale of the cubic scaling law is set by the viscous length scale

$$l_\nu \equiv \frac{\nu}{u_*}, \tag{2.14}$$

with u_* given by (2.3) , corresponding to

$$K_T^{\text{shear}} = a'_T\, \nu \left(\frac{x}{l_\nu}\right)^3, \qquad K_S^{\text{shear}} = a'_S\, \nu \left(\frac{x}{l_\nu}\right)^3, \tag{2.15}$$

where a'_T and a'_S are dimensionless constants; the prime marks them as intermediate variables, to be absorbed shortly into the constants of the flux laws. The cubic form has been extensively tested against experiments and numerical simulations of forced wall flows (Kader & Yaglom 1972). The two constants are often taken to be equal since both scalars are passive and transported by shear-induced eddies (Kader & Yaglom 1972), but DNS shows that the limiting near-wall diffusivity depends on the Pr or Sc of the scalar, because molecular diffusion damps the response of the scalar to the faster near-wall velocity fluctuations (Na & Hanratty 2000). We therefore allow a'_T and a'_S to differ.

In the buoyancy-driven regime there is very weak friction velocity driven by the plume, but the interface buoyancy anomaly Δb determines a viscous-buoyancy velocity and the corresponding viscous length,

$$u_b \equiv (\nu\, \Delta b)^{1/3}, \qquad l_b \equiv \frac{\nu}{u_b} = \left(\frac{\nu^2}{\Delta b}\right)^{1/3}. \tag{2.16}$$

Equivalently, l_b is the length at which the Grashof number $Gr = \Delta b\, l^3/\nu^2$ is unity: a parcel of fluid with buoyancy anomaly Δb and size $l < l_b$ is held back by viscosity, whereas one of size $l > l_b$ accelerates freely, so that l_b is the smallest scale at which buoyancy can drive turbulent motion and u_b is the velocity such motion attains ($u_b l_b/\nu = 1$). Therefore, l_b and u_b can be interpreted as the viscous cutoff scales of buoyancy-driven turbulence, and they play the same role as l_ν and u_* do for shear-driven turbulence in (2.14).

Note that the convective and shear-driven regimes are both characterised by a viscous length ν/u, with the velocity scale u set by the shear (u_*) or by the buoyancy forcing (Δb). The cubic law then takes the form

$$K_S^{\text{buoy}} = c'_S\, \nu \left(\frac{x}{l_b}\right)^3, \qquad K_T^{\text{buoy}} = c'_T\, \nu \left(\frac{x}{l_b}\right)^3, \tag{2.17}$$

where c'_T and c'_S are dimensionless intermediate constants.

This form of K_S^{buoy} in (2.17) recovers the KM salinity flux law: substituting it into the sublayer condition (2.11) gives $\delta_S = (\kappa_S/(c'_S\nu))^{1/3}\, l_b = \left(\kappa_S\, \nu/(c'_S\, \Delta b)\right)^{1/3}$, which is exactly the KM sublayer thickness of § 2.2 with $\gamma = (c'_S)^{1/3}$.

2.3.3. *A unified diffusivity and the resulting flux laws*

In general, both shear and buoyancy contribute to the near-wall turbulence. To combine the two cubic profiles (2.15) and (2.17) we first write them in a common form. Using $l_\nu = \nu/u_*$

and $l_b = \nu/u_b$,

$$K_\phi^{\text{shear}} = a'_\phi\,\nu\left(\frac{x}{l_\nu}\right)^3 = a'_\phi\,\nu\left(\frac{x\,u_*}{\nu}\right)^3, \qquad K_\phi^{\text{buoy}} = c'_\phi\,\nu\left(\frac{x}{l_b}\right)^3 = c'_\phi\,\nu\left(\frac{x\,u_b}{\nu}\right)^3, \tag{2.18}$$

where the subscript ϕ stands for either T or S, so that both are the same cubic law, $K_\phi \propto \nu(xu/\nu)^3$, evaluated with different velocity scales: $u = u_*$ for shear-driven and $u = u_b$ for buoyancy-driven turbulence. In both cases u is the velocity scale of the turbulent eddies at the edge of the viscous sublayer, whose imprint on the wall sets the sublayer transport, and ν/u is their size. We stress that u characterises the near-wall eddies only; farther from the ice, in the logarithmic region or the outer plume, the turbulence is governed by other scales (the distance from the wall, the plume velocity).

When shear and buoyancy act together the near-wall eddies still have a single velocity scale, which we denote u^{uni}, and the kinematic constraints at the wall that produce the cubic dependence are unchanged. The unified diffusivity is therefore again a cubic law,

$$K_\phi^{\text{uni}} = a'_\phi\,\nu\left(\frac{x\,u^{\text{uni}}}{\nu}\right)^3, \tag{2.19}$$

and the problem reduces to expressing u^{uni} in terms of u_* and u_b.

To combine the velocity scales, we appeal to the turbulent kinetic energy (TKE) budget of the near-wall layer. TKE is produced by shear, drawing energy from the mean flow, and by convection, drawing kinetic energy from the potential energy,

$$P^{\text{shear}} = -\overline{u'v'}\,\partial_x\overline{v} - \overline{u'w'}\,\partial_x\overline{w}, \qquad P^{\text{conv}} = \overline{w'b'}, \tag{2.20}$$

and in a statistically steady layer the two sources combine to balance the dissipation,

$$\varepsilon^{\text{uni}} = P^{\text{shear}} + P^{\text{conv}}. \tag{2.21}$$

The additivity of the two contributions is exact at the level of the energy budget. To turn it into a statement about u^{uni} we express each term of (2.21) through the velocity scale of the eddies that sustain it. In the viscous sublayer the eddies have velocity u and size ν/u, so their dissipation rate scales as

$$\varepsilon \sim \frac{u^3}{\nu/u} = \frac{u^4}{\nu}; \tag{2.22}$$

this is the near-wall form of the familiar estimate $\varepsilon \sim u^3/l$, and the fourth power appears because the eddy size in the sublayer is not an external length but the viscous length itself. In purely shear-driven turbulence the whole dissipation is sustained by shear production and the sublayer velocity scale is u_*, so $P_{\text{shear}} = \varepsilon^{\text{shear}} \sim u_*^4/\nu$; in purely convective turbulence it is sustained by convective production with velocity scale u_b, so $P_{\text{conv}} = \varepsilon^{\text{conv}} \sim u_b^4/\nu$. When the two coexist, each mechanism is assumed to inject energy at the rate it sustains on its own, while the total dissipation is that of eddies with the unified velocity scale u^{uni}. The budget (2.21) then reads

$$\varepsilon^{\text{uni}} = P^{\text{shear}} + P^{\text{conv}} \quad\Longrightarrow\quad \frac{\left(u^{\text{uni}}\right)^4}{\nu} \sim \frac{u_*^4}{\nu} + \frac{u_b^4}{\nu}, \qquad \text{i.e.} \qquad \left(u^{\text{uni}}\right)^4 \sim u_*^4 + u_b^4. \tag{2.23}$$

Because $K \propto u^3$ in (2.19), and with each term matched to its single-mechanism limit (2.18), this is equivalent to a statement about the turbulent diffusivities, namely that their

Rapids articles must not exceed this page length

4/3 powers add, [1]

$$K_S^{\rm uni} = \left[\left(K_S^{\rm shear}\right)^{4/3} + \left(K_S^{\rm buoy}\right)^{4/3}\right]^{3/4} = \nu x^3 \left[\left(\frac{a'_S}{l_\nu^3}\right)^{4/3} + \left(\frac{c'_S}{l_b^3}\right)^{4/3}\right]^{3/4}, \tag{2.24a}$$

$$K_T^{\rm uni} = \left[\left(K_T^{\rm shear}\right)^{4/3} + \left(K_T^{\rm buoy}\right)^{4/3}\right]^{3/4} = \nu x^3 \left[\left(\frac{a'_T}{l_\nu^3}\right)^{4/3} + \left(\frac{c'_T}{l_b^3}\right)^{4/3}\right]^{3/4}, \tag{2.24b}$$

which reduce to (2.15) for $l_\nu \ll l_b$ and to (2.17) for $l_b \ll l_\nu$. The two limits and the transition between them (§ 3.3) do not depend on the exponent in (2.23); only the shape of the crossover does.

Substituting (2.24) into (2.11) gives the sublayer thicknesses

$$\delta_S = \left(\frac{\kappa_S}{\nu}\right)^{1/3} \left[\left(\frac{a'_S}{l_\nu^3}\right)^{4/3} + \left(\frac{c'_S}{l_b^3}\right)^{4/3}\right]^{-1/4}, \qquad \delta_T = \left(\frac{\kappa_T}{\nu}\right)^{1/3} \left[\left(\frac{a'_T}{l_\nu^3}\right)^{4/3} + \left(\frac{c'_T}{l_b^3}\right)^{4/3}\right]^{-1/4}, \tag{2.25}$$

and hence, with (2.12), the unified flux laws

$$F_S = \nu^{1/3} \kappa_S^{2/3} \left[\left(\frac{a_S}{l_\nu^3}\right)^{4/3} + \left(\frac{c_S}{l_b^3}\right)^{4/3}\right]^{1/4} (S_\infty - S_b), \tag{2.26a}$$

$$F_T = \nu^{1/3} \kappa_T^{2/3} \left[\left(\frac{a_T}{l_\nu^3}\right)^{4/3} + \left(\frac{c_T}{l_b^3}\right)^{4/3}\right]^{1/4} (T_\infty - T_b). \tag{2.26b}$$

Note that we have absorbed the order-one constants from equation (2.12) into a_T, a_S, c_T and c_S, so that (2.26) now read as an equality. Our notational convention is thus: primed constants (a'_T,a'_S,c'_T, c'_S) characterize the turbulent-diffusivity profiles, while their unprimed counterparts ($a_T \sim a'_T$, $a_S \sim a'_S$ and $c_T \sim c'_T$, $c_S \sim c'_S$), which absorb these order-one prefactors, appear in the flux laws. Only the unprimed constants need to be calibrated and are set empirically based on the simulations.

Substituting the flux laws (2.26) into the interface conditions (2.1) eliminates F_T and F_S and leaves three equations for the three unknowns (T_b, S_b, $\dot{m}$), exactly as in the HJ model. The complete system is (2.1) with the fluxes given by (2.26), together with the definitions of Δb (2.4), l_ν (2.14), l_b (2.16) and u_* (2.3). Given the ambient temperature and salinity (T_∞, S_∞) and the plume velocity W, the system of equations can be solved for the melt rate

$$\dot{m} = \dot{m}\,(T_\infty,\, S_\infty,\, W)\,, \tag{2.27}$$

because l_b depends on T_b and S_b through Δb. Note that the basic structure of the closure is the same as the three-equation model in HJ and that the difference is associated with the flux laws.

[1] The relation (2.23) is a scaling, and each term carries an order-one weight. These weights need not be specified: they are fixed by requiring the unified profile to recover the single-mechanism profiles (2.18) in the two limits, which is why the constants a'_ϕ and c'_ϕ of (2.18) reappear in (2.24).

2.3.4. *Connections to previous models*

The two established models are recovered as limits of (2.26). In the low-velocity limit, a weak plume velocity W gives a small friction velocity u_*, and therefore a large viscous length l_ν, so that the buoyancy-associated term dominates (2.26). In this limit the flux laws (2.26) reduce to

$$F_S = c_S^{1/3}\,\nu^{-1/3}\,\kappa_S^{2/3}\,\Delta b^{1/3}\,(S_\infty - S_b), \tag{2.28a}$$

$$F_T = c_T^{1/3}\,\nu^{-1/3}\,\kappa_T^{2/3}\,\Delta b^{1/3}\,(T_\infty - T_b). \tag{2.28b}$$

The fluxes are independent of the plume velocity: apart from the temperature and salinity differences $T_\infty - T_b$ and $S_\infty - S_b$ themselves, they depend on the ambient state only through the interface buoyancy anomaly Δb.

Equations (2.28) are identical to the KM laws (2.6) upon identifying $\gamma = c_S^{1/3}$. However, the heat flux in (2.28)b differs from (2.9), which reflects a different treatment of how turbulence acts on the sublayers. KM treat it as intermittent: the sublayers are swept away by convective eddies and regrow by pure diffusion in between, so their thickness is set by a renewal time and $\delta \propto \kappa_T^{1/2}$, giving (2.8). Here turbulent transport extends continuously into the sublayer as the diffusivity grows away from the ice, so the thickness is set by the position where it reaches κ_T and $\delta \propto \kappa_T^{1/3}$. The two formulations therefore imply different scalings for the ratio of thermal to haline diffusive sublayer thicknesses: $\delta_T/\delta_S \propto Le^{1/2}$ in the KM model and $\delta_T/\delta_S \propto Le^{1/3}$ in our model, where $Le = \kappa_T/\kappa_S$ is the Lewis number. Howland *et al.* (2023) discussed both scaling regimes and argued that the $Le^{1/3}$ scaling is more appropriate for vertical ice faces, which is consistent with our current theory. In this paper, we could not directly test this Le-dependence because κ_T and κ_S are fixed in our simulations.

When shear dominates ($l_\nu \ll l_b$), the flux laws reduce to

$$F_S = a_S^{1/3}\,Sc^{-2/3} u_* (S_\infty - S_b), \tag{2.29a}$$

$$F_T = a_T^{1/3}\,Pr^{-2/3} u_* (T_\infty - T_b). \tag{2.29b}$$

This recovers the HJ closure (2.2) with transfer coefficients given by $\Gamma_T = a_T^{1/3}\,Pr^{-2/3}$ and $\Gamma_S = a_S^{1/3}\,Sc^{-2/3}$, where $Pr = \nu/\kappa_T$ and $Sc = \nu/\kappa_S$ are the molecular Prandtl and Schmidt numbers; this is consistent with the high-Pr, high-Sc form of Holland & Jenkins (1999).

With these connections, the flux law (2.26) can be rewritten in a form that connects directly with the existing parameterizations:

$$F_S = \left[(\Gamma_S\,u_*)^4 + \left(\Gamma_S^b\,u_b\right)^4\right]^{1/4} (S_\infty - S_b), \tag{2.30a}$$

$$F_T = \left[(\Gamma_T\,u_*)^4 + \left(\Gamma_T^b\,u_b\right)^4\right]^{1/4} (T_\infty - T_b), \tag{2.30b}$$

where $u_* = \sqrt{C_d}\,W$, $u_b = (\nu\,\Delta b)^{1/3}$, and $\Gamma_S^b = (c_S/Sc^2)^{1/3}$, $\Gamma_T^b = (c_T/Pr^2)^{1/3}$ are the transfer coefficients of the buoyancy-driven limit, defined in the same way as $\Gamma_S = (a_S/Sc^2)^{1/3}$ and $\Gamma_T = (a_T/Pr^2)^{1/3}$ for the shear-driven limit. Table 1 collects the two limits in both forms, together with the velocity and length scales that define them.

		shear-driven limit	buoyancy-driven limit
sublayer velocity scale		$u_* = \sqrt{C_d}\, W$	$u_b = (\nu\, \Delta b)^{1/3}$
sublayer length scale		$l_\nu = \nu/u_*$	$l_b = \nu/u_b$
flux law, form (2.26)	heat	$F_T = \nu\, Pr^{-2/3}\, a_T^{1/3}\, (T_\infty - T_b)/l_\nu$	$F_T = \nu\, Pr^{-2/3}\, c_T^{1/3}\, (T_\infty - T_b)/l_b$
	salt	$F_S = \nu\, Sc^{-2/3}\, a_S^{1/3}\, (S_\infty - S_b)/l_\nu$	$F_S = \nu\, Sc^{-2/3}\, c_S^{1/3}\, (S_\infty - S_b)/l_b$
flux law, form (2.30)	heat	$F_T = \Gamma_T\, u_*\, (T_\infty - T_b)$	$F_T = \Gamma_T^b\, u_b\, (T_\infty - T_b)$
	salt	$F_S = \Gamma_S\, u_*\, (S_\infty - S_b)$	$F_S = \Gamma_S^b\, u_b\, (S_\infty - S_b)$
coefficient correspondence	heat	$\Gamma_T = (a_T/Pr^2)^{1/3}$	$\Gamma_T^b = (c_T/Pr^2)^{1/3}$
	salt	$\Gamma_S = (a_S/Sc^2)^{1/3}$	$\Gamma_S^b = (c_S/Sc^2)^{1/3}$

Table 1. The two limits of the unified closure, written in the form of (2.26), in terms of the sublayer constants (a_T, a_S, c_T, c_S) and the length scales (l_ν, l_b), and in the form of (2.30), in terms of the transfer coefficients $(\Gamma_T, \Gamma_S, \Gamma_T^b, \Gamma_S^b)$ and the velocity scales (u_*, u_b). In both limits the fluxes enter the same interface conditions (2.1).

2.3.5. *Transition velocity*

The transition between the regimes occurs where the two contributions in (2.30) are comparable. Taking the salinity equation as the nominal case, this is where the two transfer velocities are equal, $\Gamma_S\, u_* = \Gamma_S^b\, u_b$, i.e.

$$u_*^{\rm cr} = \frac{\Gamma_S^b}{\Gamma_S}\, u_b, \tag{2.31}$$

so that the transition occurs when the friction velocity reaches a fixed fraction of u_b. Equivalently, since $l_\nu/l_b = u_b/u_*$, the transition occurs when the viscous length scale falls to a fixed fraction of the buoyancy length scale. In terms of the plume velocity that generates the wall stress, this gives the critical velocity

$$W^{\rm cr} = \frac{u_*^{\rm cr}}{\sqrt{C_d}} = \frac{\Gamma_S^b}{\Gamma_S}\, \frac{(\nu\, \Delta b)^{1/3}}{\sqrt{C_d}}. \tag{2.32}$$

The criterion involves only the plume velocity and the interface buoyancy anomaly, so it applies whenever a plume velocity exceeds $W^{\rm cr}$. The temperature equation gives the analogous $W_T^{\rm cr} = (\Gamma_T^b/\Gamma_T)\, (\nu\, \Delta b)^{1/3}/\sqrt{C_d}$, which differs from (2.32) only through the ratio of transfer coefficients. For the coefficients calibrated in § 3.4 the two transition velocities differ by about 6%.

For melting into water with $S_\infty = 35$ psu, $S_b \sim 20$ psu and temperatures of a few degrees Celsius, $\Delta b \sim g\beta(S_\infty - S_b) \sim 0.1\ {\rm m\,s^{-2}}$. With the transfer coefficients estimated from previous literature, $a_S \sim 10^{-3}$ (Kader & Yaglom 1972) and $c_S \sim \gamma^3 \sim 10^{-3}$ (Kerr & McConnochie 2015), so that $\Gamma_S^b/\Gamma_S \sim 1$, and $C_d = 2.5 \times 10^{-3}$, (2.32) gives

$$W^{\rm cr} \approx 0.11\ {\rm m\,s^{-1}}. \tag{2.33}$$

This estimate is higher than the previously estimated threshold of $0.04\ \mathrm{m\,s^{-1}}$ reported by McConnochie & Kerr (2017), but comes closer once the coefficients are calibrated against our simulations (§ 3.4), which give $\Gamma_S^b/\Gamma_S \approx 0.5$, $C_d \approx 1.65\times10^{-3}$ and hence $W^{\mathrm{cr}} \approx 0.07\ \mathrm{m\,s^{-1}}$ for these conditions.

2.3.6. *Summary of the unified theory*

In both regimes the turbulent heat and salt fluxes are carried to the ice by near-wall eddies of velocity u and size $l = \nu/u$. The diffusive sublayers have thicknesses proportional to l, so that the fluxes are proportional to u. The regimes are distinguished by the source of the near-wall turbulence. The mean shear of the plume sustains eddies of velocity $u_* = \sqrt{C_d}\,W$ and size $l_\nu = \nu/u_*$, whereas the buoyancy of the fresh layer at the ice sustains eddies of velocity $u_b = (\nu\Delta b)^{1/3}$ and size $l_b = \nu/u_b$. The limiting behaviour of the sublayer thickness is set by the smaller of the two lengths.

When $l_b \ll l_\nu$ (equivalently $u_* \ll u_b$) the boundary layer is buoyancy-driven: the sublayer thicknesses scale with l_b, which depends on the buoyancy anomaly Δb but not on W, so that the fluxes are independent of the plume velocity and the KM model is recovered. When $l_\nu \ll l_b$ ($u_* \gg u_b$) the boundary layer is shear-driven: the sublayer thicknesses scale with l_ν, the fluxes grow in proportion to W, and the HJ model is recovered. For a given ambient state l_b is essentially fixed, whereas l_ν shrinks as the plume accelerates with height. A meltwater plume therefore starts in the buoyancy-driven regime when the mean velocity is small, and it enters the shear-driven regime when the mean velocity accelerates to the point where the two lengths become comparable, $l_\nu \sim l_b$, and when $W \sim W^{cr}$ of (2.33).

3. Large-eddy simulations of a melting vertical ice face

In this section, we perform LES of the vertical ice-ocean interface to verify our theory, and to quantify the parameters to be used in the unified parameterization.

Our goal is to capture the transition between buoyancy-driven turbulence and shear-driven turbulence in a melt-driven plume. As discussed in the introduction, both regimes arise naturally within the melt plume along a vertical ice face (Wells & Worster 2008): close to the bottom of the domain the plume is weak and the near-wall turbulence is buoyancy-driven; sufficiently far downstream the plume velocity is large and the near-wall turbulence is expected to become shear-driven (Wells & Worster 2008; Jenkins 2011). However, simulating this spatial development directly requires a tall domain and near-wall resolution sufficient to capture the small-scale turbulence near the ice-ocean interfaces, a combination that is computationally prohibitive. We therefore adopt a small-domain configuration that focuses on the near-wall boundary layer, using periodic boundary conditions in the vertical direction to convert the spatially developing problem into a temporally evolving one. A similar setting has been previously used to study the NCBL (Ke *et al.* 2020, 2021, 2023, 2026).

3.1. *Simulation setting*

We consider seawater of temperature T, salinity S and velocity $\boldsymbol{u} = (u, v, w)$ adjacent to a flat, vertical ice face, in the configuration sketched in Figure 2a: x is normal to the ice, y is spanwise and z is vertical, anti-parallel to gravity. The flow is governed by the Navier-Stokes equations under the Boussinesq approximation,

$$\frac{\partial \boldsymbol{u}}{\partial t} + \boldsymbol{u}\cdot\boldsymbol{\nabla}\boldsymbol{u} = -\boldsymbol{\nabla}p + b\,\hat{\boldsymbol{z}} + \nu\nabla^2\boldsymbol{u}, \qquad \boldsymbol{\nabla}\cdot\boldsymbol{u} = 0, \tag{3.1a}$$

$$\frac{\partial T}{\partial t} + \boldsymbol{u} \cdot \boldsymbol{\nabla} T = \kappa_T \nabla^2 T, \qquad \frac{\partial S}{\partial t} + \boldsymbol{u} \cdot \boldsymbol{\nabla} S = \kappa_S \nabla^2 S, \tag{3.1b}$$

where p is the pressure divided by the reference density ρ_0. The buoyancy is related to temperature and salinity through a linear equation of state,

$$b = g\left[\alpha\left(T - T_\infty\right) - \beta\left(S - S_\infty\right)\right], \tag{3.2}$$

so that $b = 0$ in the ambient fluid with uniform temperature and salinity, T_∞ and S_∞, respectively. Molecular and thermodynamic parameter values representative of cold seawater are used throughout and are collected in table 2. In this setting, the dimensional form of the equations and variables is more convenient as it allows a coupling with the ice-ocean boundary condition (2.1).

Periodic boundary conditions are applied in the vertical (z) and spanwise (y) directions. The ice-ocean interface lies on the left boundary, where (2.1) is imposed with $F_T = \kappa_T \partial T/\partial x$ and $F_S = \kappa_S \partial S/\partial x$ evaluated as the diffusive fluxes at the interface. Because the diffusive sublayers are well resolved in the simulations, the melt rate emerges without any wall model or parameterization of the interfacial fluxes and can be used to test the theories. A no-slip velocity condition is applied at the ice face, whereas a free-slip condition is employed at the right boundary. To be consistent with the theory, the ice face is held fixed at $x = 0$ and its retreat is not simulated. Wall-resolved simulations that include the retreating boundary find that it thins the haline sublayer by 10–15 % while leaving temperature and momentum profiles essentially unaffected (Zhao *et al.* 2026).

The simulations are initialized with uniform temperature and salinity T_∞ and S_∞ throughout the domain. Melting supplies cold, fresh water at the ice face, and because the domain is periodic in the vertical there is no outflow to remove it. As a result, the water in the domain cools and freshens with time, and entrainment acts only to thicken the meltwater plume rather than to establish the steady balance of the spatially developing case as in Figure 2b. No steady state is therefore reached, and the plume accelerates and thickens continuously in time.

The simulations are performed with Oceananigans (Ramadhan *et al.* 2020), a GPU-accelerated incompressible finite-difference solver. The domain has size $L_x \times L_y \times L_z = 2.5\ \mathrm{m} \times 1\ \mathrm{m} \times 2\ \mathrm{m}$, and the grid contains $256 \times 512 \times 512$ points. The wall-normal grid (x direction) is stretched, with a minimum spacing $\Delta x_{\min} = 0.07$ mm at the ice and $\Delta x_{\max} = 30$ mm in the far field; the grid is uniform in y and z with $\Delta y = 1.96$ mm and $\Delta z = 3.91$ mm. In the wall-normal direction $\Delta x_{\min}$ resolves the thin haline diffusive sublayer ($\delta_S \approx 1$ mm) with multiple grid points, so that the interfacial fluxes and the melt rate are carried by resolved molecular diffusion. The relatively coarse resolution in the far field does not significantly affect our primary focus in the boundary layer. In the wall-parallel directions, the most stringent requirements for Δy and Δz arise in the shear-driven regime: the characteristic viscous length $l_\nu = \nu/u_*$ shrinks as the plume accelerates, so the late shear-driven stage of each simulation is the hardest to resolve. For the velocity field, our resolution reaches the standards of classical DNS of wall-bounded turbulence ($\Delta z < 12\, l_\nu$, $\Delta y < 7\, l_\nu$ as in Kim *et al.* (1987); Moin & Mahesh (1998)) up to $W \approx 0.14\ \mathrm{m\,s^{-1}}$, where W is the maximum plume velocity. However, the high Pr and Sc lead to very small Batchelor scales for temperature and salinity, and resolving them throughout the domain is computationally infeasible (Yeung *et al.* 2004; Donzis *et al.* 2010). We therefore make no attempt to resolve the scalar microscales away from the ice. Instead, the scalar variance cascading below the grid scale is removed by the numerical dissipation of the WENO advection scheme (Silvestri *et al.* 2024), which thereby acts as an implicit subgrid-scale

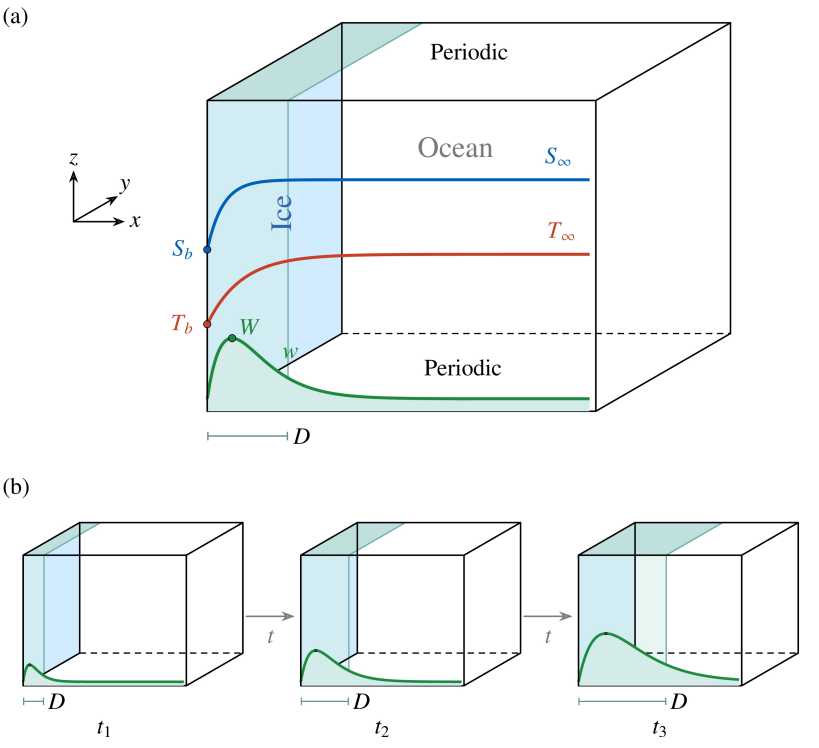


Figure 2. Schematic of the LES configuration. (a) The melting ice face (shaded plane) lies at $x = 0$, and periodic boundary conditions are applied in the along-ice directions y and z. The sketched curves illustrate the mean profiles of salinity (blue), temperature (red) and vertical velocity (green), the last of which peaks close to the ice at the plume velocity W; the shaded band indicates the meltwater plume of width D. (b) The same domain at three successive times. Since the domain is periodic in z, the plume does not grow with height but widens and accelerates in time, so that D and W depend on t alone.

closure at the smallest resolved scales. For this reason our simulations should be regarded as implicit LES rather than DNS. The sensitivity of the results to resolution is discussed in Appendix A.

Eight simulations are performed, spanning the ambient temperatures and salinities listed in table 2. The reference case (case 1) has $(T_\infty, S_\infty) = (0\,^\circ\text{C}, 35\text{ psu})$, representative of cold sea water in polar oceans; three further cases reduce the ambient salinity from 30 to 20 psu at fixed temperature (cases 2–4), and four cases vary the ambient temperature between -1 and $4\,^\circ\text{C}$ at a fixed salinity of 34.5 psu (cases 5–8). The interface conditions and transition velocities predicted for each case by the unified model, which require the calibrated parameters of table 3, are collected in table 4 in § 3.4.

3.2. *Basic Flow Evolution*

The basic flow evolution can be seen in the $x - z$ slices of Figure 3: the meltwater at the ice-ocean interface drives the meltwater plume, which accelerates and expands as it entrains ambient water. The plume is characterized by positive mean vertical velocity adjacent to the ice, and its growth can be described by the plume velocity W and plume width D, defined by:

$$W(t) = \max[\overline{w}(x,t)], \tag{3.3a}$$

(*a*) Physical constants

ν	1.8×10^{-6} m^2 s^{-1}	λ_1	-5.73×10^{-2} °C psu^{-1}
κ_T	1.4×10^{-7} m^2 s^{-1}	λ_2	8.32×10^{-2} °C
κ_S	1×10^{-9} m^2 s^{-1}	λ_3	-7.53×10^{-4} °C dbar^{-1}
$Pr=\nu/\kappa_T$	14	c_w	3974 J kg^{-1} °C^{-1}
$Sc=\nu/\kappa_S$	1800	L	3.35×10^5 J kg^{-1}
α	3.87×10^{-5} °C^{-1}	g	9.81 m s^{-2}
β	7.86×10^{-4} psu^{-1}	P	500 dbar

(*b*) Ambient conditions

Case	1 (Reference)	2	3	4	5	6	7	8
T_∞ (°C)	0.0	0.0	0.0	0.0	−1.0	0.0	2.0	4.0
S_∞ (psu)	35.0	30.0	25.0	20.0	34.5	34.5	34.5	34.5

Table 2. Simulation parameters. (*a*) Molecular and thermodynamic constants, representative of cold seawater, used in all simulations. (*b*) Ambient temperature T_∞ and salinity S_∞ of the eight cases.

$$D(t)=\frac{1}{W(t)}\int_0^\infty \overline{w}(x',t)dx' \tag{3.3b}$$

where $\bar{\cdot}$ denotes an average over y and z. The time evolution of $\overline{w}(x)$ and $\overline{T}(x)$ can be more clearly seen in Figure 4(a,b), and the resulting time evolution of $W(t)$ and $D(t)$ is shown in Figure 4(c,d), for the reference simulation (case 1 of table 2).

The growth of W and D follows from the two basic ingredients of plume theory (Morton *et al.* 1956). The plume accelerates because the wall continuously supplies it with buoyancy, and it thickens because it entrains ambient fluid. For a spatially developing wall plume fed by a vertically distributed source of buoyancy, this theory with a constant entrainment coefficient gives a thickness growing linearly with height and a velocity growing as its one-third power, $D\propto z$ and $W\propto z^{1/3}$ (Wells & Worster 2008; Cooper & Hunt 2010; McConnochie & Kerr 2016; Parker *et al.* 2021). Our plume is instead periodic in the vertical and develops in time (cf. Abedin *et al.* 2009; Ke *et al.* 2020), so that W and D increase with t rather than with z. The temporal evolution of the boundary layer allows us to evaluate the theory for a range of W and D values.

The plume dynamics here are more complex than in classical plume theory. The wall buoyancy flux is not prescribed and begins to depend on W once the boundary layer becomes shear-driven, and the entrainment into the plume need not be the same in the two regimes. A plume model that spans the transition would have to account for both sources of buoyancy. Such a plume model that predicts the evolution of W and D is beyond the scope of this paper which focuses on boundary layers, and we leave this for future work.

A useful organizing principle, here and in the analyses that follow, is that the outer plume dynamics and the near-wall boundary-layer dynamics are distinct, but coupled. This two-layer structure is well established for natural convection boundary layers (George & Capp 1979; Tsuji & Nagano 1988; Wells & Worster 2008; Ke *et al.* 2020, 2021). The two layers are coupled through the maximum plume velocity. The time evolution of W is determined by the plume dynamics (Morton *et al.* 1956); turbulence in the near-wall boundary layer is controlled by W, but this turbulence also feeds back on the plume evolution by influencing the heat and salt fluxes and viscous stress at the boundary. Figure 4(c,d) characterizes the outer plume, whose influence on the melting is felt entirely through W.

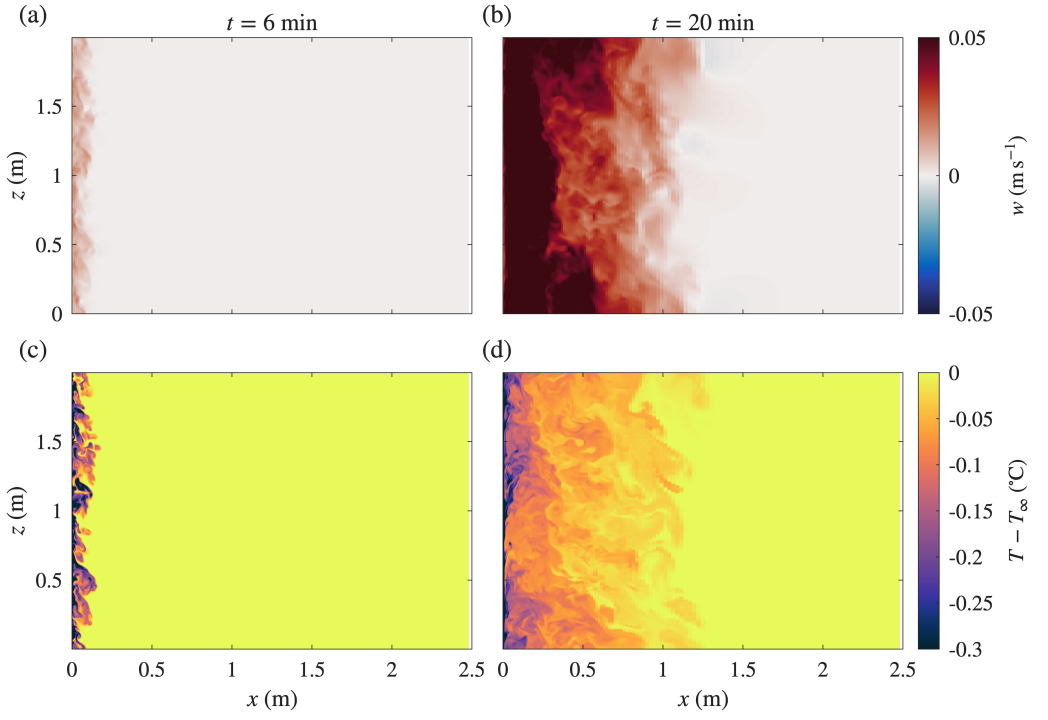


Figure 3. Instantaneous slices in the x–z plane from the reference simulation ($T_\infty = 0\,^\circ$C, $S_\infty = 35$ psu): (a,b) vertical velocity w at $t = 6$ min and $t = 20$ min; (c,d) temperature anomaly $T - T_\infty$ at the same two times. The buoyant meltwater plume adjacent to the ice face at $x = 0$ accelerates and thickens with time as it entrains ambient fluid.

The finite computational domain places restrictions on the interpretation of the simulations. Plume-scale diagnostics such as the time-evolution of $D(t)$ and $W(t)$ are only meaningful before t_{dom}, when the plume reaches the outer boundary (Figure 4). However, the boundary layer dynamics, which only depend on the local W and the ice-ocean interface, are unaffected even after $t > t_{\mathrm{dom}}$. Since our focus here is the boundary layer dynamics, we retain data beyond t_{dom}, and mark t_{dom} in the figures below where such data appear.

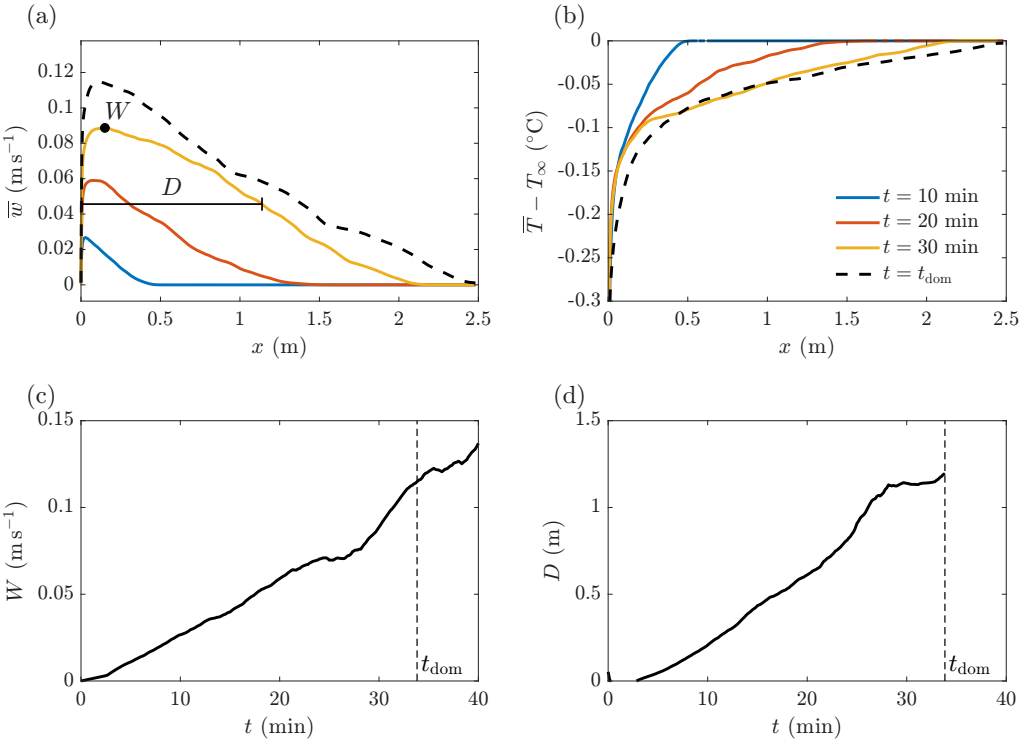


Figure 4. Evolution of the horizontally averaged flow in the reference simulation. (*a*) Mean vertical velocity $\overline{w}(x)$ and (*b*) mean temperature anomaly $\overline{T} - T_\infty$ at $t = 10$, 20 and 30 min and at $t = t_{\mathrm{dom}}$ (dashed); the graphical construction of the plume velocity W and the plume width D defined in (3.3) is indicated in (*a*). (*c*,*d*) Time series of $W(t)$ and $D(t)$, which characterize the outer plume dynamics; the outer flow couples to the near-wall boundary layer through W alone (see text). The vertical dashed line marks t_{dom}, the time at which the plume reaches the outer boundary of the domain.

3.3. *Regime transition*

Figure 5(a) shows the evolution of the melt rate with time. The domain is initially filled with warm water, so the melt rate is at first very high and falls rapidly as a cold, fresh laminar layer forms at the ice face. This laminar stage is double-diffusive: because heat diffuses much faster than salt, the thin fresh layer next to the ice rises while the thicker, cooled but still salty layer outside it sinks, the bidirectional flow observed at melting ice walls by Josberger & Martin (1981) and analysed by Carey & Gebhart (1982). The laminar flow becomes unstable at $t_{\mathrm{turb}} \approx 2.3$ min. The melt rate then recovers as turbulence erodes the cold, fresh layer accumulated during the laminar stage and brings warm, salty water back towards the ice. Turbulent fluxes are established within a few minutes, and from $t \approx 6$ min the melt rate settles into a plateau, consistent with convection-driven turbulence that is independent of the plume velocity. The plateau is not perfectly flat: the melt rate overshoots slightly and then declines slowly. The slight time-dependence of the melt rate during this stage can be explained by the slow molecular diffusion of salt. The salinity profile inside the diffusive haline sublayer, where there is no turbulent transport, can adjust only by molecular diffusion, on a time scale $\delta_S^2/\kappa_S \sim 10$ min. When turbulence sets in it transports salty water close to the ice, leaving the diffusive haline sublayer thinner than its equilibrium thickness. The sublayer then relaxes by diffusion, so that the salt flux at the ice and the melt rate lag the flux delivered by the turbulence just outside the sublayer. This lag is comparable to the duration of the buoyancy-driven stage, and the wall flux never fully settles before the transition to shear-driven turbulence (§3.4).

To illustrate the flow structures in two regimes, Figure 6 shows the vertical velocity in a y–z plane 1 cm from the ice-ocean interface, a visualization inspired by the wall-parallel snapshots of Ke *et al.* (2023). At $t = 5$ min, when turbulence is driven primarily by the convective buoyancy flux, the flow is organized into a collection of small buoyant plumes. A similar state is found in vertical natural convection at moderate Grashof number, where the turbulence is sustained by the plume-like structures rather than by the near-wall shear (Ng *et al.* 2017; Ke *et al.* 2023). At $t = 33$ min, when shear production is the dominant source of turbulence, the snapshot instead shows thin elongated streaks, the classical signature of shear-driven wall-bounded turbulence (Kline *et al.* 1967).

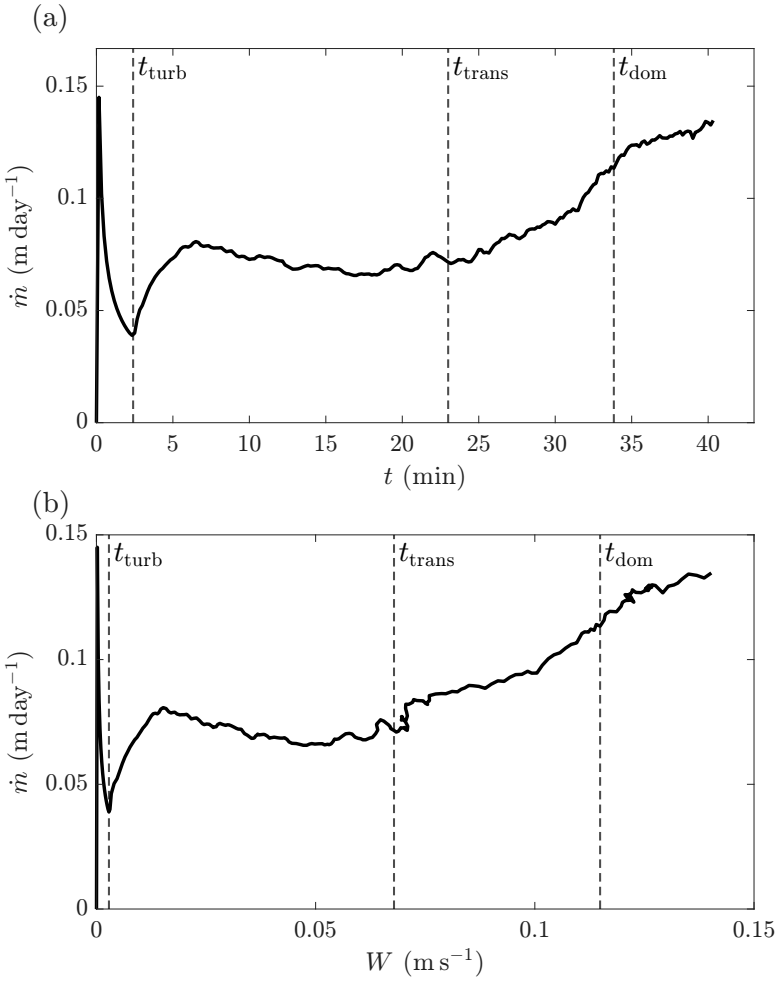


Figure 5. Melt rate $\dot{m}$ in the reference simulation, plotted (*a*) as a function of time and (*b*) as a function of the plume velocity W. Vertical dashed lines mark the transition to turbulence (t_{turb}), the transition from the buoyancy-driven to the shear-driven regime (t_{trans}) and the time at which the plume width reaches the domain size (t_{dom}). The melt rate is approximately constant in the buoyancy-driven regime and increases with W once the boundary layer becomes shear-driven.

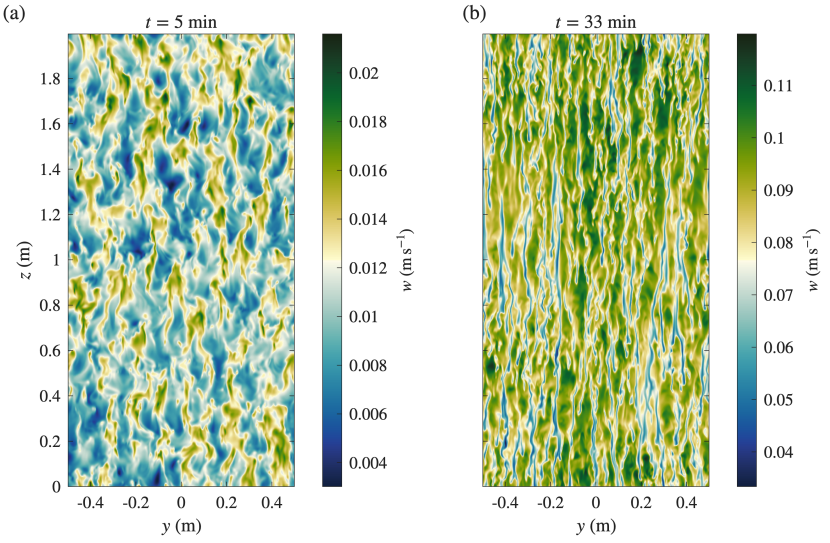


Figure 6. Snapshots of the vertical velocity w in a y–z plane located 1 cm from the ice-ocean interface, for the reference simulation. (*a*) t = 5 min, in the buoyancy-driven regime: the near-wall flow is organized into small-scale coherent buoyant plumes. (*b*) t = 33 min, in the shear-driven regime: the flow is organized into elongated streamwise (vertical) streaks characteristic of sheared wall-bounded turbulence. Note the different colour scales in the two panels.

The transition between the two flow regimes can also be seen from the perspective of the vertical momentum budget. In the quasi-steady state for melting, we find that the tendency for the vertical velocity is small, and the momentum budget for the vertical velocity $\overline{w}(x)$ reduces to:

$$0 \approx \frac{\partial \overline{w}}{\partial t} = \partial_x(\nu \overline{w}_x) + b - \partial_x(\overline{u'w'}) \tag{3.4}$$

Integrating from 0 to x leads to the accumulated momentum budget. Defining the wall stress $\tau_{\text{wall}} \equiv \nu \overline{w}_x|_{x=0}$, the viscous stress $\tau_\nu(x) \equiv \nu \overline{w}_x(x)$, the Reynolds stress $\tau_u(x) \equiv -\overline{u'w'}(x)$ and the integrated buoyancy $\tau_b(x) \equiv \int_0^x \overline{b}(x')dx'$, this reads

$$\tau_{\text{wall}} \approx \tau_\nu(x) + \tau_u(x) + \tau_b(x), \tag{3.5}$$

so that the total stress $\tau_{\text{total}} \equiv \tau_\nu + \tau_u + \tau_b$ is independent of x. This is verified in our simulation in Figure 7(a). The slightly higher τ_{total} compared with τ_{wall} reflects a weak overall acceleration of the plume, consistent with the system being in a slowly evolving quasi-steady state.

The viscous stress τ_ν decreases from τ_{wall} at the ice to near zero at $x \approx 2$ cm, where $\overline{w}_x = 0$; τ_b rises to more than half of τ_{wall} within the first millimetre, the haline sublayer, whereas τ_u only becomes appreciable beyond $x \approx 2$ mm, so that in between the momentum supplied by buoyancy is transmitted to the ice viscously. Since τ_ν is negligible beyond $x \approx 2$ cm, we quantify the buoyancy and Reynolds-stress contributions to the wall stress through $\tau_{\text{wall}} \approx \tau_b(2\,\text{cm}) + \tau_u(2\,\text{cm})$, so that the stress at the ice-ocean interface is contributed by both the thin buoyancy boundary layer (contributed mainly by the salinity), and the turbulent Reynolds stress which reflects the strength of the shear-driven turbulence. The evolution of τ_{wall}, $\tau_u(2\,\text{cm})$ and $\tau_b(2\,\text{cm})$, is shown in Figure 7b. The wall stress, τ_{wall}, is dominated by τ_b in the convection-driven regime, while τ_u increases with W, until it becomes comparable with the buoyancy contribution near the transition. Throughout the turbulent stage, τ_u follows the quadratic drag law $\tau_u = C_d W^2$ with a best-fit $C_d = 1.65 \times 10^{-3}$ (dashed curve), whereas τ_{wall}, which also carries τ_b and remains finite as $W \to 0$, does not. This is why u_* is based on the Reynolds stress rather than on the interfacial stress (§ 2.1).

The momentum budget connects directly to the transition criterion of Section 2, because the contributions to the wall stress scale with the two velocity scales of the theory:

$$\tau_u \simeq u_*^2, \qquad \tau_b \approx \Delta b\, \delta_S \sim \Delta b\, l_b = u_b^2, \tag{3.6}$$

where the first follows from the definition of u_* (§ 2.1), and the second follows because at large Schmidt number the buoyancy anomaly is confined to the diffusive sublayer, whose thickness δ_S scales with $l_b = \nu/u_b$ in the convection-driven regime. The transition criterion $u_* \sim u_b$ of (2.31) is therefore equivalent to $\tau_u \sim \tau_b$. The transition occurs when the Reynolds stress, growing quadratically with W, becomes comparable with the buoyancy contribution. The ratio τ_u/τ_b at the transition is about 0.15 (Figure 7(b)) due to the non-dimensional coefficients in (2.31) and the two stresses become equal only near t_{dom}. The transition is also visible in τ_b itself, which is constant in the convection-driven regime and decreases beyond it. Since τ_b is essentially the interfacial buoyancy anomaly times δ_S, and the interfacial anomaly changes little across the transition, this decrease reflects the thinning of the sublayer: δ_S scales with l_ν in the shear-driven regime and therefore shrinks as W increases, for the same reason that the melt rate increases.

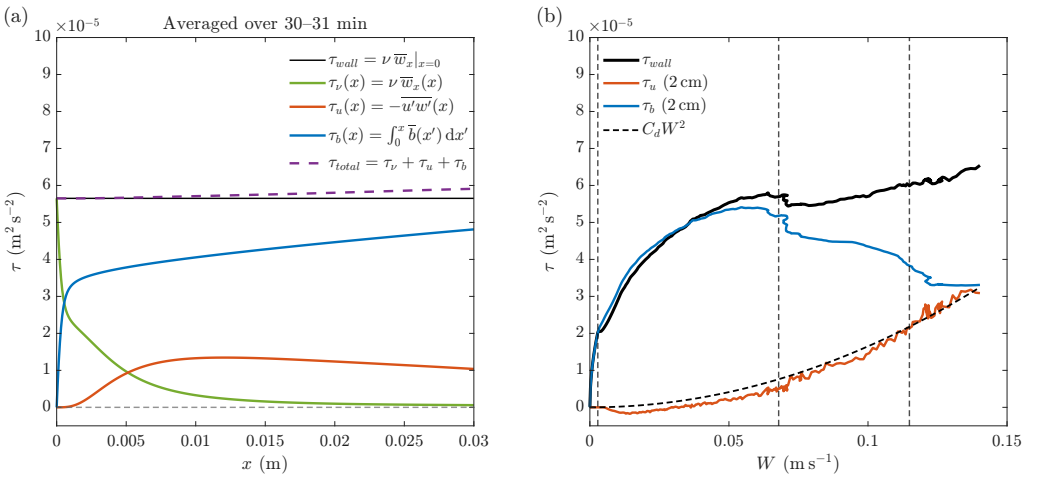


Figure 7. Decomposition of the vertical momentum budget (3.5) in the reference simulation. (*a*) Wall-normal profiles of the viscous stress $\tau_\nu(x) = \nu\,\overline{w}_x(x)$, the Reynolds stress $\tau_u(x) = -\overline{u'w'}(x)$, the integrated buoyancy $\tau_b(x) = \int_0^x \overline{b}(x')\,\mathrm{d}x'$ and their sum τ_{total}, averaged over t = 30–31 min; the horizontal line marks the wall stress $\tau_{\mathrm{wall}} = \nu\,\overline{w}_x|_{x=0}$. The viscous stress falls to near zero by $x \approx 2$ cm, beyond which $\tau_{\mathrm{wall}} \approx \tau_b + \tau_u$. (*b*) Evolution of τ_{wall}, τ_u and τ_b, evaluated at $x = 2$ cm, as functions of the plume velocity W; the dashed curve shows the quadratic drag law C_dW^2 fitted to τ_u, with the best-fit $C_d = 1.65 \times 10^{-3}$, and the vertical dashed lines mark t_{turb}, t_{trans} and t_{dom} as in figure 5.

3.4. *Comparison with the theoretical prediction*

We now test whether the simulations are consistent with the unified model of § 2.3. The reference simulation is used to determine the four dimensionless parameters $(\Gamma_S, \Gamma_T, \Gamma_S^b, \Gamma_T^b)$. These parameters, together with the drag coefficient diagnosed in § 3.3, is then used to predict the melt rate in all the other cases.

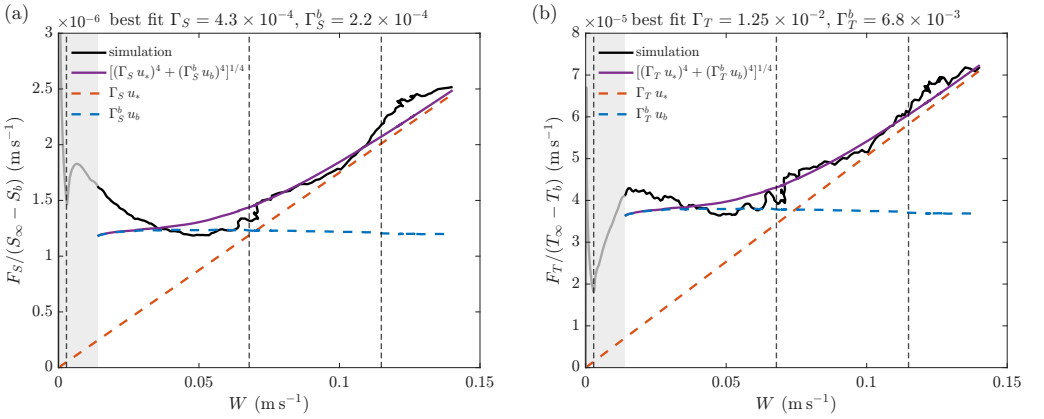


Figure 8. Determination of the four transfer coefficients of the unified flux law (2.30) from the reference simulation. The simulated transfer velocities $F_S/(S_\infty - S_b)$ (*a*) and $F_T/(T_\infty - T_b)$ (*b*) (black) are compared with the unified law $[(\Gamma u_*)^4 + (\Gamma^b u_b)^4]^{1/4}$ (purple) and its two limits, the shear-driven Γu_* (red dashed) and the buoyancy-driven $\Gamma^b u_b$ (blue dashed). The coefficients are obtained by a least-squares fit of the unified law to the transfer velocities for $t > 6$ min, giving $\Gamma_S = 4.3 \times 10^{-4}$, $\Gamma_S^b = 2.2 \times 10^{-4}$, $\Gamma_T = 1.25 \times 10^{-2}$ and $\Gamma_T^b = 6.8 \times 10^{-3}$. The grey band marks the first six minutes, during which the boundary layer is still adjusting from the laminar stage, which is excluded from the fit. The vertical dashed lines mark t_{turb}, t_{trans} and t_{dom} as in figure 5.

Γ_S	Γ_T	Γ_S^b	Γ_T^b	C_d
4.3×10^{-4}	1.25×10^{-2}	2.2×10^{-4}	6.8×10^{-3}	1.65×10^{-3}

Table 3. Best-fit transfer coefficients of the unified flux law (2.30), obtained by a least-squares fit to the reference simulation as illustrated in figure 8, together with the drag coefficient C_d diagnosed in § 3.3. The shear-driven coefficients (Γ_S, Γ_T) and the buoyancy-driven coefficients (Γ_S^b, Γ_T^b) are defined in table 1. All are dimensionless, independent of the ambient state (T_∞, S_∞) and of the plume velocity W, and are used unchanged in all the comparisons of § 3.4.

Figure 8 illustrates how the parameters are determined: the simulated transfer velocities $F_S/(S_\infty - S_b)$ and $F_T/(T_\infty - T_b)$ are compared with the unified law (2.30), and the four transfer coefficients are obtained by a least-squares fit. The first 6 minutes of evolution, shown in grey, are excluded from the fit because the boundary layer is still adjusting from the laminar stage (Section 3.3). The transfer velocities continue to decline slowly throughout the subsequent convection-driven stage, introducing uncertainties in the fitted coefficients (Γ_S^b, Γ_T^b). The fitted values are listed in table 3. All parameters are dimensionless and independent of (T_∞, S_∞, W). The same fit applied to the other seven simulations gives values within 10% of the parameter values given in the table.

With the parameters in 3, we solve (2.1) together with the unified flux laws (2.30), to obtain the melt rate $\dot{m}(T_\infty, S_\infty, W)$. In the classical three-equation formulation the transfer coefficients $\gamma_T \equiv F_T/(T_\infty - T_b)$ and $\gamma_S \equiv F_S/(S_\infty - S_b)$ are constant, so eliminating $\dot{m}$ reduces the system to a quadratic in the interface salinity S_b with a closed-form root. In the unified model γ_T and γ_S are themselves functions of S_b, through the buoyancy-flux dependence of the transfer coefficients, which destroys the quadratic structure and leaves a nonlinear scalar residual $R(S_b) = 0$. We therefore solve for S_b numerically with a bracketed Brent method, and then derive the melt rate.

The solutions for each case are compared with all eight simulations in Figure 9(a,b). With a single parameter set the prediction reproduces the melt rate across both families of simulations, in both regimes. The prediction does reasonably well in all cases, but performs less well in the buoyancy-driven regime when T_∞ and S_∞ are large. Specifically, the prediction does not capture the time-dependent melt rate during the buoyancy-driven regime when, as noted above, the haline sublayer takes $\sim$ 10 minutes to equilibrate through molecular diffusion. This weak time-dependence is likely a result of the temporally developing simulation configuration. Unfortunately this makes it difficult to quantify the sharpness of the regime transition, and as a result we cannot validate the precise exponent in (2.30).

Beyond the melt rate, the predicted interface temperature and salinity track the values diagnosed from the simulations closely in every case (not shown for brevity). This is a nontrivial consistency check since (T_b, S_b) emerge from the coupled interface conditions rather than being imposed. Perhaps most importantly, the predicted transition velocity, marked by the filled circles in Figure 9(a,b), is consistent with the regime transition seen in the simulations. In the theory the transition occurs when the friction velocity u_* reaches the critical value $(\Gamma_S^b/\Gamma_S)\, u_b$ (2.32), and the two are compared in Figure 9(c,d). The magnitudes of the characteristic velocity scales are worth noting. The buoyancy velocity u_b is 4–7 mm s^{-1} across the cases, while u_* grows linearly with the plume velocity and reaches about 6 mm s^{-1} by the end of the simulations. The transition occurs once $u_* \simeq$ 2–3.5 mm s^{-1}. Because Δb varies only weakly through (T_b, S_b), this critical value is nearly fixed for each case, and the predicted transition is where u_* crosses it as the plume

Case	T_∞ (°C)	S_∞ (psu)	S_b (psu)	T_b (°C)	Δb (m s^{-2})	W^{cr} (m s^{-1})
1 (Reference)	0.0	35.0	22.3	−1.57	9.8×10^{-2}	0.071
2	0.0	30.0	19.7	−1.42	7.8×10^{-2}	0.066
3	0.0	25.0	17.1	−1.27	6.1×10^{-2}	0.060
4	0.0	20.0	14.2	−1.11	4.4×10^{-2}	0.054
5	−1.0	34.5	26.6	−1.82	6.1×10^{-2}	0.060
6	0.0	34.5	22.0	−1.55	9.6×10^{-2}	0.070
7	2.0	34.5	15.9	−1.20	1.4×10^{-1}	0.080
8	4.0	34.5	12.2	−0.99	1.7×10^{-1}	0.085

Table 4. Ambient conditions (T_∞, S_∞) together with the interface salinity S_b, interface temperature T_b, interface buoyancy anomaly $\Delta b = g(\beta(S_\infty - S_b) - \alpha(T_\infty - T_b))$ and transition velocity W^{cr} predicted by the unified closure for the eight cases of table 2, using the parameters of table 3. The interface values are evaluated in the buoyancy-controlled (free-convection) limit, in which they are independent of W; W^{cr} is the transition velocity given by (2.32).

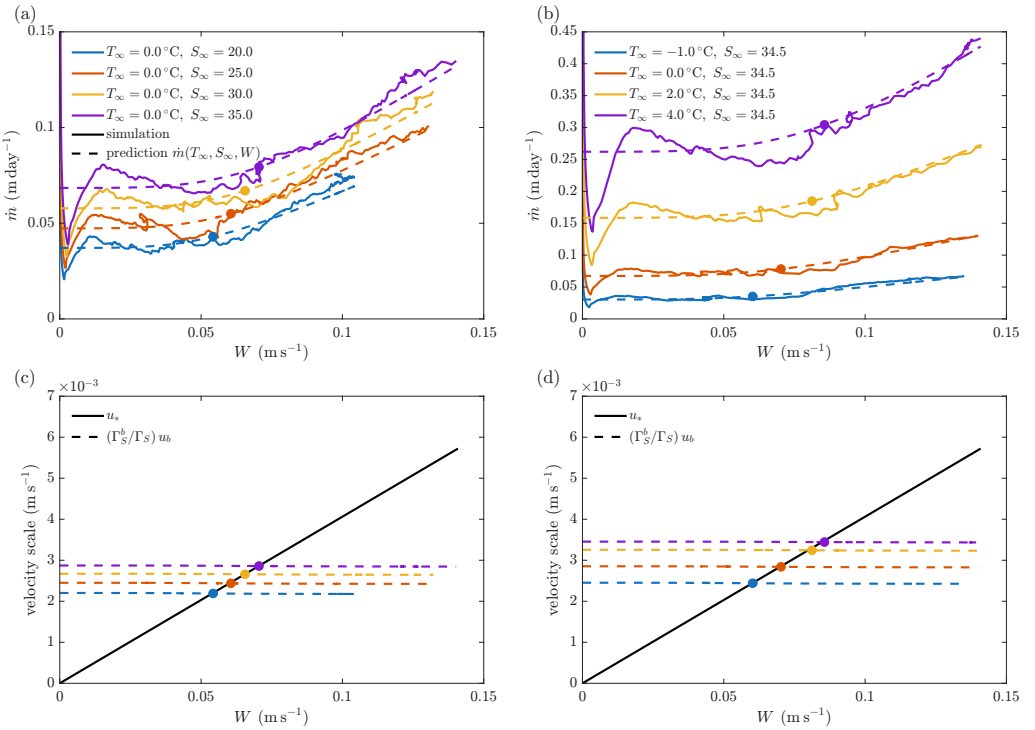


Figure 9. Comparison between the simulated melt rates and the unified parameterization, using the single set of parameters of table 3 fitted to the reference simulation. (*a*) Simulations with fixed $T_\infty = 0\,°C$ and $S_\infty = 20$–35 psu; (*b*) simulations with fixed $S_\infty = 34.5$ psu and $T_\infty = -1$ to $4\,°C$. Solid curves show the simulated melt rate as a function of the plume velocity W, dashed curves the theoretical prediction $\dot{m}(T_\infty, S_\infty, W)$, and filled circles the predicted transition velocity. (*c*,*d*) The competing length scales $l_\nu/a_S^{1/3}$ (solid) and $l_b/c_S^{1/3}$ (dashed) for the same two sets of simulations; their crossover gives the predicted transition velocities marked in (*a*,*b*).

accelerates. The predictions for all eight cases are collected in table 4. Note that T_∞ and S_∞ jointly influence (T_b, S_b), and thereby Δb and W^{cr}. Across the eight cases Δb spans close to a factor of four, but u_b depends only on $\Delta b^{1/3}$, and the corresponding transition velocities fall in the range 0.06–0.08 m s^{-1} in the parameter space relevant for fjords ($S > 30$).

4. Conclusions and discussion

We have developed a boundary-layer theory for the melt rate at a vertical ice–ocean interface beneath a buoyant plume which resulted in a unified model describing the melt rate (2.30), and tested it against boundary-layer-resolving large-eddy simulations. The theory assumes that the turbulent diffusivity grows as the cube of the distance from the ice, with an amplitude set by the near-wall eddies, which have a velocity u and a size ν/u. When the turbulence is driven by the shear associated with the plume, these scales are the friction velocity u_* and the viscous length $l_\nu = \nu/u_*$. When turbulence is driven by convection near the ice face, the characteristic velocity and length scales are the buoyancy velocity $u_b = (\nu\,\Delta b)^{1/3}$ and the buoyancy length $l_b = \nu/u_b = (\nu^2/\Delta b)^{1/3}$.

The result can be interpreted in two equivalent ways. In terms of lengths, the diffusive sublayers, whose thicknesses set the fluxes, are controlled by l_b when the plume is weak and by l_ν when the plume is strong. The scale l_b is essentially fixed by the ambient state, whereas l_ν shrinks as the plume accelerates. The flow transitions from buoyancy-driven to shear-driven when the viscous length falls to about twice the buoyancy length. In terms of velocities, the flux laws take the algebraic form of the three equation model described in Holland & Jenkins (1999) (referred to here as the HJ model), with the transfer velocity $\Gamma\,u_*$ replaced by one that never falls below $\Gamma^b u_b$. The transition between buoyancy-driven and shear-driven turbulence occurs when $u_* \approx 0.5\,u_b$. The velocity-independent convective law of Kerr & McConnochie (2015) (referred to here as the KM model) and the shear-driven HJ model are recovered as limits, and the transition corresponds to a plume velocity of 0.06–0.08 m s^{-1} for conditions relevant to glaciers in fjords.

The large-eddy simulations resolve the diffusive sublayers at a melting vertical ice face and, by exploiting vertical periodicity, follow a plume driven by melting alone as it transitions from the buoyancy-driven into the shear-driven regime within a single run. With one set of coefficients fitted to a single reference simulation, the parameterization predicts the melt rate in all eight cases, spanning ambient temperatures of -1 to 4 °C and salinities of 20–35 psu. The plume velocity at the regime transition is well-predicted by the theory. The flow in the buoyancy-driven regime is characterised by coherent plumes, while streamwise streaks characterise the shear-driven regime. Given the ambient temperature and salinity and the plume velocity, the predicted melt rate matches the simulations across the buoyancy-driven, transitional and shear-driven regimes.

Unlike previous criteria based on a Rayleigh number built on the distance along the ice face (Wells & Worster 2008; Kerr & McConnochie 2015; McConnochie & Kerr 2017), the transition criterion in our theory depends only on local flow properties, specifically the plume velocity and the interface buoyancy anomaly. The regime transition predicted by our theory is not highly sensitive to the properties of the ambient water in fjords. For example, since the transition velocity scales as $\Delta b^{1/3}$, the factor-of-three difference in thermal driving between Atlantic-water-filled fjords in southeast Greenland, near 4 °C, and colder fjords in the north, near 0 °C, shifts the transition velocity by less than a factor of 1.5. Which regime a given part of an ice face is in is therefore decided mainly by the strength of the plume.

For many applications a simpler expression for the melt rate may suffice. The transition between the two regimes is rapid. In the theory this follows from the fourth-power combination in (2.30), and the simulations also show a sharp regime transition. A closure may therefore simply take the larger of the shear-driven and buoyancy-driven transfer velocities, as in Schulz *et al.* (2022) and Zhao *et al.* (2024, 2026). Our model can also be viewed as a version of the HJ model with a floor on the friction velocity of about half the buoyancy velocity u_b, which for typical ambient salinities is nearly constant and

corresponds to a plume velocity of roughly $0.07\ \mathrm{m\,s^{-1}}$. With a constant floor, the HJ model retains its closed-form solution and is straightforward to implement in existing models.

To apply the parameterization, one needs the plume velocity close to the ice and the ambient temperature and salinity. Fjord-scale ocean models resolve neither the boundary layer nor the plume, so they do not provide this velocity and the closure cannot be used in them directly. The plume velocity has to come from one of three sources. First, it can be measured: ice-mounted instruments such as the Meltstake (Nash *et al.* 2024; Weiss *et al.* 2025) record the velocity within tens of centimetres of the ice together with the melt rate, and so offer a direct test of the closure (although the velocity maximum of a thin plume is difficult to resolve acoustically so close to the ice (Weiss *et al.* 2025)). Second, it can be taken from simulations that resolve the plume but not the diffusive sublayers (e.g. Zhao *et al.* 2024), for which the closure acts as a wall model for the melt rate. Third, it can be predicted from far-field hydrography with a plume model of the Morton *et al.* (1956) type, which is how melt rates at glacier termini are usually estimated (e.g. Sutherland *et al.* 2019). This route, however, requires a more accurate plume model than those in current use. Existing plume models (e.g. Jenkins 2011; Cowton *et al.* 2015) assume that the melting is shear-driven everywhere along the ice face and compute it with the HJ flux laws, so they account neither for the buoyancy-driven regime nor for the transition. A plume model that does is left for future work.

Several further simplifications remain. The drag coefficient was calibrated on the maximum velocity of the plume, whereas plume models carry a width-averaged velocity. The maximum and mean plume velocities differ by an order-one factor that must be accounted for when the closure is driven by a plume model. The ice face is vertical and smooth, whereas real ice faces are inclined, rough and sculpted by the melting itself (Mondal *et al.* 2019; Zhao *et al.* 2026; Pegler & Davies Wykes 2020; Couston *et al.* 2021). Roughness may modify C_d, although in the shear-driven simulations of Couston *et al.* (2021) the channels generated by melting did not significantly change it. The forcing is steady, whereas unsteady near-ice flows appear to enhance melting (Weiss *et al.* 2025).

The present model considers only shear generated by the buoyant plume and does not account for externally driven shear. Observations near glacier termini and icebergs reveal horizontal currents, waves, and eddies whose velocities can exceed those of the plume and which appear to contribute substantially to observed melting (Jackson *et al.* 2020; Weiss *et al.* 2025). The transition criterion derived here therefore cannot be assumed to apply unchanged when these ambient flows are present. Zhao *et al.* (2026) have taken a first step toward understanding this coupled problem through DNSs with an imposed horizontal current, showing that the melt rate increases above its convective value as the imposed velocity increases. A general theory accounting for both plume-generated and externally driven shear remains to be developed. The present model provides the theoretical basis for the buoyancy-driven case against which the effects of these ambient flows can be assessed.

Acknowledgements. This work is from the GIANT project, funded by the Advanced Research + Invention Agency (ARIA) Forecasting Tipping Points Programme (GIANT project; SCOP-PR01-P028). GIANT Contribution No. GIANT-008. The authors thank the members of the GIANT project team and the Atmosphere-Ocean Dynamics group at DAMTP for helpful discussions.

Declaration of interests The authors report no conflict of interest.

Use of generative AI During manuscript preparation, the authors used Claude Fable 5.1 to write scripts used to plot simulation data and to suggest edits for a draft of the manuscript to improve the clarity of the text. The authors reviewed all suggestions, re-edited the text, checked the plotting code and verified the figures against the underlying data. The authors take responsibility for the accuracy and integrity of the final manuscript.

Appendix A. Sensitivity of the simulations to grid resolution

As discussed in §3.1, the grid does not resolve the Batchelor scales of temperature and, in particular, salinity. Scalar variance cascading below the grid scale is instead removed by the implicit numerical dissipation of the WENO advection scheme, which acts as an effective subgrid closure. Unresolved scalar variance does not by itself imply that the fluxes are misrepresented: the wall-normal flux is carried by the near-wall eddies of the velocity field, which the grid resolves to the standard of wall-bounded DNS (§3.1), whereas the finest scalar structures carry variance rather than flux. It is nevertheless important to verify that the quantities central to this study, specifically the melt rate and the boundary-layer statistics from which the transfer coefficients and the sublayer thicknesses are inferred, are not sensitive to the grid resolution.

Because the simulations are run on a single GPU, memory constraints prohibit a uniform refinement of the grid in all three directions. We therefore test the resolution dependence in two complementary steps. First, the grid is refined in the spanwise and streamwise directions while keeping the wall-normal resolution fixed, giving $256 \times 768 \times 768$ grid points; this tests whether the results are limited by the resolution of the turbulence in the plane parallel to the ice face. Second, the grid is refined in the wall-normal direction, giving $512 \times 512 \times 512$ grid points with the same tanh stretching described in §3.1; this tests the sensitivity to the resolution of the diffusive sublayers adjacent to the ice. Both refined simulations use $T_\infty = -0.12\,^\circ\mathrm{C}$, $S_\infty = 34.5\,\mathrm{psu}$ and a reference pressure of 1000 dbar, with all other parameters identical to those listed in table 2.

Figure 10(*a*,*b*) compares the melt rate $\dot{m}$ and the plume velocity W as functions of time for the three grids. In the buoyancy-driven regime, neither depends sensitively on the resolution, indicating that the near-wall structures controlling the melt rate in this regime are adequately resolved. Some dependence emerges in the shear-driven regime and becomes more pronounced as the velocity increases. This is expected: as W, and hence u_*, grows, the viscous length $l_\nu = \nu/u_*$ decreases and the near-wall shear layer becomes progressively harder to resolve. The simulations are therefore not fully converged in the shear-driven regime at the largest velocities reached. This affects the fitting of the transfer coefficients, but the resulting variation in Γ_T and Γ_S across the three grids is less than 10 %.

Figure 10(*c*,*d*) shows the corresponding sublayer thicknesses δ_T and δ_S and their ratio. Both thicknesses, and in particular the haline sublayer, whose thickness is comparable to the lateral grid spacing, are indistinguishable across the three grids in both regimes, and the ratio δ_T/δ_S is unchanged.

References

Abedin, Mohammad Zoynal, Tsuji, Toshihiro & Hattori, Yasuo 2009 Direct numerical simulation for a time-developing natural-convection boundary layer along a vertical flat plate. *International Journal of Heat and Mass Transfer* **52** (19-20), 4525–4534.

Carey, Van P. & Gebhart, Benjamin 1982 Transport near a vertical ice surface melting in saline water: some numerical calculations. *Journal of Fluid Mechanics* **117**, 379–402.

Chapman, D. R. & Kuhn, G. D. 1986 The limiting behaviour of turbulence near a wall. *J. Fluid Mech.* **170**, 265–292.

Cheesewright, R. 1968 Turbulent natural convection from a vertical plane surface. *Trans. ASME J. Heat Transfer* **90**, 1–8.

Cooper, Paul & Hunt, Gary R 2010 The ventilated filling box containing a vertically distributed source of buoyancy. *Journal of Fluid Mechanics* **646**, 39–58.

Couston, L.-A., Hester, E., Favier, B., Taylor, J. R., Holland, P. R. & Jenkins, A. 2021 Topography generation by melting and freezing in a turbulent shear flow. *J. Fluid Mech.* **911**, A44.

Cowton, Tom, Slater, Donald, Sole, Andrew, Goldberg, Dan & Nienow, Peter 2015 Modeling the impact of glacial runoff on fjord circulation and submarine melt rate using a new subgrid-scale parameterization for glacial plumes. *J. Geophys. Res. Oceans* **120** (2), 796–812.

Cusack, J. M., Jackson, R. H., Nash, J. D., Skyllingstad, E., Pettit, E. C., Sutherland, D. A., Motyka, R. J. & Amundson, J. M. 2023 Internal gravity waves generated by subglacial discharge: Implications for tidewater glacier melt. *Geophysical Research Letters* **50** (12), e2022GL102426.

Donzis, D. A., Sreenivasan, K. R. & Yeung, P. K. 2010 The Batchelor spectrum for mixing of passive scalars in isotropic turbulence. *Flow Turbul. Combust.* **85**, 549–566.

Gayen, B., Griffiths, R. W. & Kerr, R. C. 2016 Simulation of convection at a vertical ice face dissolving into saline water. *J. Fluid Mech.* **798**, 284–298.

George, W. K. & Capp, S. P. 1979 A theory for natural convection turbulent boundary layers next to heated vertical surfaces. *Intl J. Heat Mass Transfer* **22**, 813–826.

Grossmann, S. & Lohse, D. 2000 Scaling in thermal convection: a unifying theory. *J. Fluid Mech.* **407**, 27–56.

Hewitt, I. J. 2020 Subglacial plumes. *Annu. Rev. Fluid Mech.* **52**, 145–169.

Holland, D. M. & Jenkins, A. 1999 Modeling thermodynamic ice–ocean interactions at the base of an ice shelf. *J. Phys. Oceanogr.* **29**, 1787–1800.

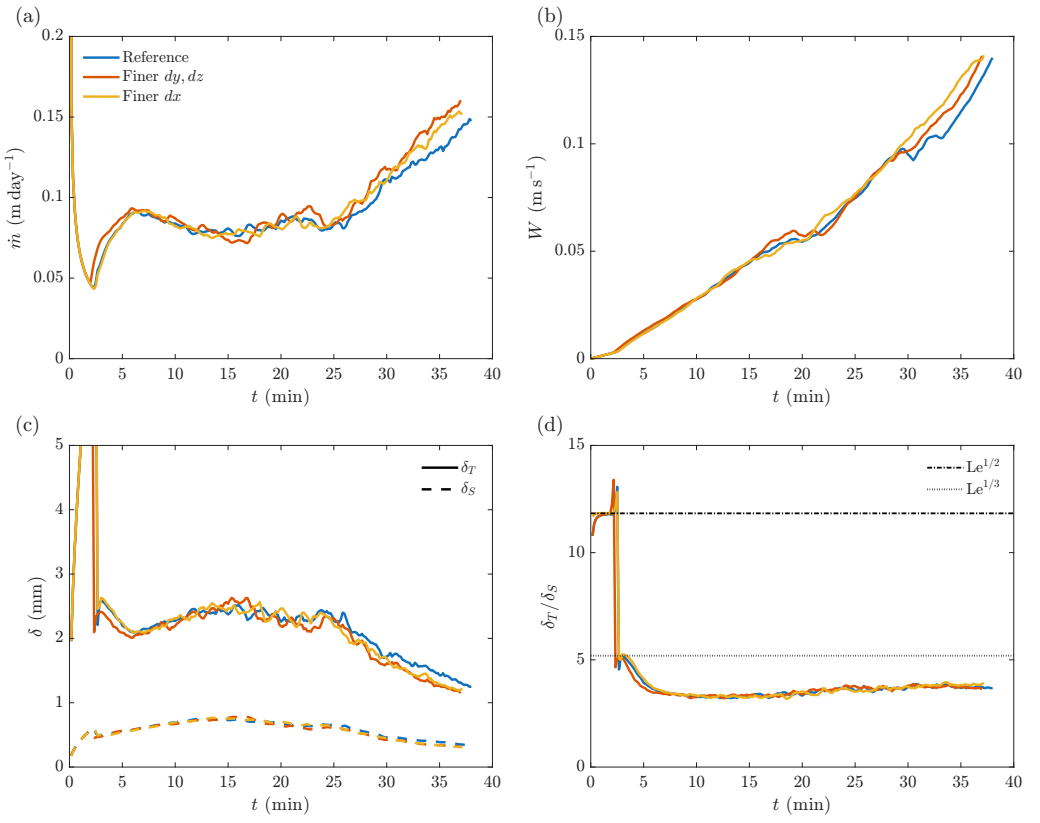


Figure 10. Sensitivity of the simulation results to grid resolution, for the case with $T_\infty = -0.12\,^\circ$C, $S_\infty = 34.5$ psu and a reference pressure of 1000 dbar. (*a*) Melt rate $\dot{m}$, (*b*) plume velocity W, (*c*) thermal (solid) and haline (dashed) sublayer thicknesses and (*d*) their ratio, as functions of time, for the reference grid ($256\times512\times512$), the grid refined in the spanwise and streamwise directions ($256\times768\times768$) and the grid refined in the wall-normal direction ($512\times512\times512$). In (*d*) the dash-dotted and dotted lines mark $\mathrm{Le}^{1/2}$ and $\mathrm{Le}^{1/3}$.

Howland, C. J., Verzicco, R. & Lohse, D. 2023 Double-diffusive transport in multicomponent vertical convection. *Phys. Rev. Fluids* **8**, 013501.

Jackson, R. H., Nash, J. D., Kienholz, C., Sutherland, D. A., Amundson, J. M., Motyka, R. J., Winters, D., Skyllingstad, E. & Pettit, E. C. 2020 Meltwater intrusions reveal mechanisms for rapid submarine melt at a tidewater glacier. *Geophys. Res. Lett.* **47**, e2019GL085335.

Jackson, R. H., Shroyer, E. L., Nash, J. D., Sutherland, D. A., Carroll, D., Fried, M. J., Catania, G. A., Bartholomaus, T. C. & Stearns, L. A. 2017 Near-glacier surveying of a subglacial discharge plume: implications for plume parameterizations. *Geophys. Res. Lett.* **44**, 6886–6894.

Jenkins, A. 2011 Convection-driven melting near the grounding lines of ice shelves and tidewater glaciers. *J. Phys. Oceanogr.* **41**, 2279–2294.

Jenkins, A., Nicholls, K. W. & Corr, H. F. J. 2010 Observation and parameterization of ablation at the base of Ronne Ice Shelf, Antarctica. *J. Phys. Oceanogr.* **40**, 2298–2312.

Josberger, E. G. & Martin, S. 1981 A laboratory and theoretical study of the boundary layer adjacent to a vertical melting ice wall in salt water. *J. Fluid Mech.* **111**, 439–473.

Kader, B. A. & Yaglom, A. M. 1972 Heat and mass transfer laws for fully turbulent wall flows. *Intl J. Heat Mass Transfer* **15**, 2329–2351.

Kasagi, N., Tomita, Y. & Kuroda, A. 1992 Direct numerical simulation of passive scalar field in a turbulent channel flow. *Trans. ASME J. Heat Transfer* **114**, 598–606.

Ke, J., Komiya, A., Armfield, S. W. & Williamson, N. 2026 On the role of moderate Prandtl numbers in vertical natural convection. *J. Fluid Mech.* **1029**, A37.

Ke, J., Williamson, N., Armfield, S. W. & Komiya, A. 2023 The turbulence development of a vertical natural convection boundary layer. *J. Fluid Mech.* **964**, A24.

Ke, J., Williamson, N., Armfield, S. W., Komiya, A. & Norris, S. E. 2021 High Grashof number turbulent natural convection on an infinite vertical wall. *J. Fluid Mech.* **929**, A15.

Ke, J., Williamson, N., Armfield, S. W., Norris, S. E. & Komiya, A. 2020 Law of the wall for a temporally evolving vertical natural convection boundary layer. *J. Fluid Mech.* **902**, A31.

Kerr, R. C. & McConnochie, C. D. 2015 Dissolution of a vertical solid surface by turbulent compositional convection. *J. Fluid Mech.* **765**, 211–228.

Kim, J., Moin, P. & Moser, R. 1987 Turbulence statistics in fully developed channel flow at low Reynolds number. *J. Fluid Mech.* **177**, 133–166.

Kimura, S., Holland, P. R., Jenkins, A. & Piggott, M. 2014 The effect of meltwater plumes on the melting of a vertical glacier face. *J. Phys. Oceanogr.* **44**, 3099–3117.

Kline, S. J., Reynolds, W. C., Schraub, F. A. & Runstadler, P. W. 1967 The structure of turbulent boundary layers. *J. Fluid Mech.* **30**, 741–773.

Magorrian, S. J. & Wells, A. J. 2016 Turbulent plumes from a glacier terminus melting in a stratified ocean. *J. Geophys. Res. Oceans* **121**, 4670–4696.

McConnochie, C. D. & Kerr, R. C. 2016 The turbulent wall plume from a vertically distributed source of buoyancy. *J. Fluid Mech.* **787**, 237–253.

McConnochie, C. D. & Kerr, R. C. 2017 Testing a common ice–ocean parameterization with laboratory experiments. *J. Geophys. Res. Oceans* **122**, 5905–5915.

McPhee, M. G., Maykut, G. A. & Morison, J. H. 1987 Dynamics and thermodynamics of the ice/upper ocean system in the marginal ice zone of the Greenland Sea. *J. Geophys. Res.* **92**, 7017–7031.

Moin, P. & Mahesh, K. 1998 Direct numerical simulation: a tool in turbulence research. *Annu. Rev. Fluid Mech.* **30**, 539–578.

Mondal, M., Gayen, B., Griffiths, R. W. & Kerr, R. C. 2019 Ablation of sloping ice faces into polar seawater. *J. Fluid Mech.* **863**, 545–571.

Monin, A. S. & Yaglom, A. M. 1971 *Statistical Fluid Mechanics: Mechanics of Turbulence, Vol. 1*. MIT Press.

Morton, B. R., Taylor, G. I. & Turner, J. S. 1956 Turbulent gravitational convection from maintained and instantaneous sources. *Proc. R. Soc. Lond. A* **234**, 1–23.

Mouginot, Jérémie, Rignot, Eric, Bjørk, Anders A., van den Broeke, Michiel, Millan, Romain, Morlighem, Mathieu, Noël, Brice, Scheuchl, Bernd & Wood, Michael 2019 Forty-six years of Greenland Ice Sheet mass balance from 1972 to 2018. *Proceedings of the National Academy of Sciences* **116** (19), 9239–9244.

Murphree, E. V. 1932 Relation between heat transfer and fluid friction. *Ind. Engng Chem.* **24**, 726–736.

Na, Y. & Hanratty, T. J. 2000 Limiting behavior of turbulent scalar transport close to a wall. *Intl J. Heat Mass Transfer* **43** (10), 1749–1758.

Nakao, K., Hattori, Y. & Suto, H. 2017 Numerical investigation of a spatially developing turbulent natural convection boundary layer along a vertical heated plate. *Intl J. Heat Fluid Flow* **63**, 128–138.

Nash, J. D., Weiss, K., Wengrove, M. E., Osman, N., Pettit, E. C., Zhao, K. & others 2024 Turbulent dynamics of buoyant melt plumes adjacent near-vertical glacier ice. *Geophys. Res. Lett.* **51**, e2024GL108790.

Ng, C. S., Ooi, A., Lohse, D. & Chung, D. 2015 Vertical natural convection: application of the unifying theory of thermal convection. *J. Fluid Mech.* **764**, 349–361.

Ng, C. S., Ooi, A., Lohse, D. & Chung, D. 2017 Changes in the boundary-layer structure at the edge of the ultimate regime in vertical natural convection. *J. Fluid Mech.* **825**, 550–572.

Ovall, Bridget, Jackson, Rebecca H, Nash, Jonathan D, Zhao, Ken, Abib, Nicole, Cusack, Jesse M, Skyllingstad, Eric, Sutherland, David A & Pettit, Erin C 2025 Velocity observations in an upwelling subglacial discharge plume reveal links between entrainment and ice morphology. *Journal of Geophysical Research: Oceans* **130** (11), e2025JC022902.

Parker, D. A., Burridge, H. C., Partridge, J. L. & Linden, P. F. 2021 Vertically distributed wall sources of buoyancy. part 1. unconfined. *Journal of Fluid Mechanics* **907**, A15.

Pegler, S. S. & Davies Wykes, M. S. 2020 Shaping of melting and dissolving solids under natural convection. *J. Fluid Mech.* **900**, A35.

Ramadhan, A., Wagner, G. L., Hill, C., Campin, J.-M., Churavy, V., Besard, T., Souza, A., Edelman, A., Ferrari, R. & Marshall, J. 2020 Oceananigans.jl: Fast and friendly geophysical fluid dynamics on GPUs. *J. Open Source Softw.* **5**, 2018.

Schulz, K., Nguyen, A. T. & Pillar, H. R. 2022 An improved and observationally-constrained melt rate parameterization for vertical ice fronts of marine terminating glaciers. *Geophys. Res. Lett.* **49**, e2022GL100654.

Schwertfirm, F. & Manhart, M. 2007 DNS of passive scalar transport in turbulent channel flow at high Schmidt numbers. *Intl J. Heat Fluid Flow* **28**, 1204–1214.

Shaya, M. F., Nash, J. D., Pettit, E. C., Amundson, J. M., Jackson, R. H., Sutherland, D. A. & Winters,

D. 2025 Calving as a source of acute and persistent kinetic energy to enhance submarine melting of tidewater glaciers. *Geophysical Research Letters* **52** (19), e2025GL117900.

Silvestri, S., Wagner, G. L., Campin, J.-M., Constantinou, N. C., Hill, C. N., Souza, A. & Ferrari, R. 2024 A new WENO-based momentum advection scheme for simulations of ocean mesoscale turbulence. *J. Adv. Model. Earth Syst.* **16**, e2023MS004130.

Sutherland, D. A., Jackson, R. H., Kienholz, C., Amundson, J. M., Dryer, W. P., Duncan, D., Eidam, E. F., Motyka, R. J. & Nash, J. D. 2019 Direct observations of submarine melt and subsurface geometry at a tidewater glacier. *Science* **365**, 369–374.

Tsuji, T. & Nagano, Y. 1988 Characteristics of a turbulent natural convection boundary layer along a vertical flat plate. *Intl J. Heat Mass Transfer* **31**, 1723–1734.

Tsuji, T. & Nagano, Y. 1989 Velocity and temperature measurements in a natural convection boundary layer along a vertical flat plate. *Exp. Therm. Fluid Sci.* **2**, 208–215.

Versteegh, T. A. M. & Nieuwstadt, F. T. M. 1999 A direct numerical simulation of natural convection between two infinite vertical differentially heated walls: scaling laws and wall functions. *Intl J. Heat Mass Transfer* **42**, 3673–3693.

Vreugdenhil, C. A. & Taylor, J. R. 2019 Stratification effects in the turbulent boundary layer beneath a melting ice shelf: insights from resolved large-eddy simulations. *J. Phys. Oceanogr.* **49**, 1905–1925.

Vreugdenhil, C. A., Taylor, J. R., Davis, P. E. D., Nicholls, K. W., Holland, P. R. & Jenkins, A. 2022 The ocean boundary layer beneath Larsen C Ice Shelf: insights from large-eddy simulations with a near-wall model. *J. Phys. Oceanogr.* **52**, 1903–1926.

Warner, C. Y. & Arpaci, V. S. 1968 An experimental investigation of turbulent natural convection in air at low pressure along a vertical heated flat plate. *Intl J. Heat Mass Transfer* **11**, 397–406.

Weiss, K. J., Nash, J. D., Wengrove, M. E., Osman, N., Cohen, N. F., Jackson, R. H. & others 2025 Direct measurement of glacier ice melt: boundary layer details are critical for submarine melt prediction at near-vertical ice faces. *Geophys. Res. Lett.* **52**, e2025GL114952.

Weiss, Kaelan J. & others 2026 Small-scale observations of submarine melt rate and ice-ocean boundary layer forcing at a marine-terminating glacier. Manuscript submitted to Science.

Wells, A. J. & Worster, M. G. 2008 A geophysical-scale model of vertical natural convection boundary layers. *J. Fluid Mech.* **609**, 111–137.

Yeung, P. K., Xu, S., Donzis, D. A. & Sreenivasan, K. R. 2004 Simulations of three-dimensional turbulent mixing for Schmidt numbers of the order 1000. *Flow Turbul. Combust.* **72**, 333–347.

Zhao, K. X., Chor, T., Skyllingstad, E., Nash, J., Rosevear, M. & McConnochie, C. 2026 Direct numerical simulations of ice–ocean boundary turbulence. *arXiv preprint arXiv:2603.19542* .

Zhao, K. X., Skyllingstad, E. D. & Nash, J. D. 2024 Improved parameterizations of vertical ice–ocean boundary layers and melt rates. *Geophys. Res. Lett.* **51**, e2023GL105862.